Polyethylenimine-DNA Nanoparticles Under Endosomal Acidification and Implication to Gene Delivery

Subhamoy Mahajan and Tian Tang*

Department of Mechanical Engineering, University of Alberta, Edmonton, Alberta, Canada

Email: tian.tang@ualberta.ca

Abstract

Non-viral gene delivery using polyethylenimine (PEI) has shown tremendous promise as a therapeutic technique. Through the formation of nanoparticles (NPs), PEIs protect genetic material such as DNA from degradation. Escape of the NPs from endosomes and lysosomes is facilitated by PEI's buffering capacity over a wide range of pH. However, little is known about the effects of endosomal acidification on the morphology of the NPs. In this work, large-scale coarse-grained simulations performed to mimic endosomal acidification reveal that NPs undergo a resizing process that is highly dependent on the N/P ratio (ratio of PEI nitrogen to DNA phosphate) at which they are prepared. With a low N/P ratio, NPs further aggregate after endosomal acidification, whereas with a high N/P ratio they dissociate. The mechanisms behind such NP resizing and its consequences on endosomal escape and nuclear trafficking are discussed. Based on the findings, suggestions are made on the PEI architecture that may enhance NP dissociation driven by endosomal acidification.

Keywords: molecular dynamics, biopolymers, non-viral gene delivery, pH-sensitive nanoparticle, transition diagram, *in-silico* microscopy.

1. Introduction

Gene therapy treats diseases by introducing genetic material such as DNA into malignant cells.[1] For a successful delivery, DNAs have to overcome several barriers such as cell association, cellular uptake, endosomal escape, and nuclear trafficking.[2–4] Specialized carriers are required to overcome these barriers since DNAs, by themselves, are susceptible to enzyme degradation along the delivery pathway.[5,6] Viral carriers such as adenovirus are often used because their cell-proliferating molecular machinery has been honed by evolution, making them highly efficient.[7] This is, however, accompanied by the risk of immunogenicity which needs to be managed.[8] One solution is to use synthetically manufactured non-viral carriers, whose efficacy can be tweaked by changing its molecular structure, mass, chemical composition, *etc*.[2] Polyethylenimine (PEI) has stood out as one of the most studied non-viral carriers due to its high efficacy and versatility.[9]

PEI-based DNA delivery follows an endocytic pathway, where the PEI-DNA nanoparticles (NPs) are trapped in early endosomes after cellular uptake.[10] Early endosomes are continuously acidified by proton pumps (H^+-ATPase), leaving the DNAs vulnerable to acidic digestion.[11,12] PEI's high efficacy arises from its ability to protect DNAs by absorbing protons[3] and escape from endosomes with the DNAs.[13] The endosomal escape mechanism is not fully understood but is widely accredited to the "proton sponge" hypothesis.[13–15] Under this hypothesis, PEIs act as a buffer to absorb protons (like a sponge), which results in more protons pumped into the endosome. Consequently, there is an electrostatics-driven entry of counterions[16] (such as chloride) and osmotic entry of water.[13,14] Such influxes cause endosomal swelling, and if substantial, it can lead to endosomal burst or localized rupture which release all the NPs into the cytoplasm.[13,17,18] Experimental work by Vermeulen *et al*.[17] further proposed an burst criterion for the endosome

based on its size. Other proposed endosomal escape mechanisms are associated with PEI's membrane damaging properties.[10,19]

Several all-atom (AA) molecular dynamics (MD) simulations have been performed to supplement experimental understanding of endosomal escape. AA-MD studies of PEI-DNA complexation and PEI-mediated DNA aggregation have explored pH-dependent stability of the complexes.[20–22] Complexes at endosomal pH were found to be more stable and compact than those at physiological pH.[20–22] However, the length (10-15 nm) and time (20-60 ns) scales that can be studied in AA-MD simulations are significantly smaller than those in experiments. In comparison, coarse-grained (CG)-MD simulations allow larger length and time scales while capable of maintaining key molecular perspectives. Among the CG techniques, Martini can achieve length scale of up to 50 nm and time scale of up to 80 μs.[23,24] It is particularly attractive for biomolecular simulations because it contains forcefields of many biomolecules and produces good qualitative agreement with experiments.[23,24] Martini CG-MD have been used to study the complexation patterns of large DNA and polycations,[25] and large-scale aggregation of several PEIs and DNAs.[26] Endosomal escape has also been investigated using Martini CG-MD, although not for PEI-DNA delivery systems.[27,28] Tian and Ma[27] explored the membrane destabilizing properties of polyamidoamine (PAMAM) at physiological and endosomal pH, while Bruininks et al.[28] probed fusion mechanism between lipoplexed DNAs and a model endosomal membrane. Other than CG-MD simulations, the "proton sponge" hypothesis has been examined using continuum-level theories. Yang and May[29] modeled the "proton sponge" character of linear PEIs using Poisson-Boltzmann theory, whereas Freeman et al.[30] studied acidification and protonation kinetics of a dendritic polymer inside an endosome using rate equations.

As endosomal acidification is expected to alter the morphology of endosomes (swell, rupture, burst, *etc*.), the same is possible for PEI-DNA NPs. For example, upon endosomal acidification, decondensation of plasmid DNAs[18,31] and dissociation of oligonucleotides from NPs[18] have been reported based on fluorescence microscopy measurements. The detailed mechanism involved in such processes is unclear due to the spatio-temporal resolution limit of fluorescence microscopy.[32,33] Furthermore, the location where genetic materials are released from the NPs is not well agreed upon and has been proposed to occur in the endosome[18], in the cytoplasm[31], or not occur at all[6,34] (i.e., NPs stay intact in the nucleus). This warrants a theoretical study exploring the effects of endosomal acidification on NP properties.

Further motivation comes from our previous work[26] where PEI-DNA aggregation under physiological pH was studied using Martini CG-MD simulations at different PEI/DNA number ratios α (proportional to the N/P ratio which is the ratio of PEI nitrogen to DNA phosphate). The results hinted that endosomal acidification might alter NP properties depending on the α value at which the NPs were prepared. In particular, aggregation of NPs was promoted by diffusion and hindered by the *specific repulsion* (electrostatic repulsion between two NPs, where the net charge of each NP is normalized by the number of DNAs in it), which scales quadratically with α.[26] It is worth noting that the term "specific repulsion" here refers to an intrinsic property similar to "specific gravity" and "specific density"; it is not related to specific interactions such as those between ligands and receptors. For low and high α, the specific repulsion between NPs was high leading to the formation of small NPs, while large NPs were formed at moderate α. At a critical α (α_c), where the DNAs were just neutralized by the PEIs, the specific repulsion was the lowest and NP aggregation (quantified by the average number of DNAs in the NPs) the highest; as shown schematically in **Figure 1** (grey curve). We hypothesize that similar phenomenon exists at

endosomal pH (**Figure 1**, black curve), and that α_c at endosomal pH (α_c^e) is less than that at physiological pH (α_c^p) because PEIs are more protonated at endosomal pH and hence require smaller α to neutralize the DNAs. According to this hypothesis, NPs prepared at physiological pH with $\alpha < \alpha_c^e$ would aggregate further when placed in the endosomal environment (upward arrow; **Figure 1**), and conversely would dissociate when prepared with $\alpha > \alpha_c^p$ (downward arrow; **Figure 1**). The present work uses Martini CG-MD simulations to explore the validity of this hypothesis, which we refer to as the *acidic resizing* of NPs, and its implications to gene delivery.

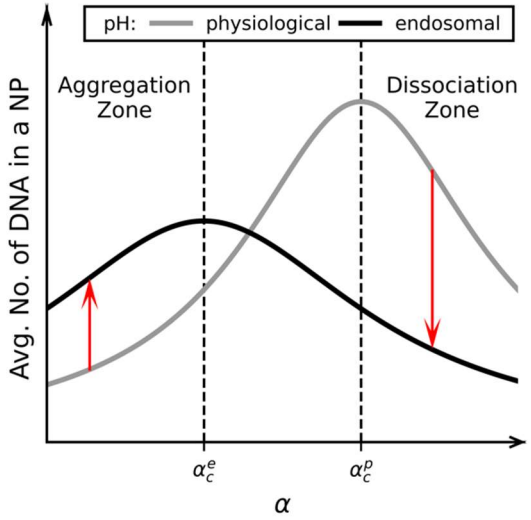

Figure 1. Proposed schematic representation of the average number of DNAs in a NP *vs.* PEI/DNA number ratio (α) under physiological (grey) and endosomal (black) pH. Dashed vertical lines mark the critical α values at which the average number of DNAs in a NP is maximized: (left) under endosomal pH; (right) under physiological pH.

2. Materials and Methods

2.1 Simulations

Martini coarse-grained (CG) molecular dynamics (MD) simulations were performed for both aggregation and acidification. Specifics for the two types of simulations can be found in **Section 2.1.1** and **Section 2.1.2** respectively, with common details described below.

The DNA simulated was the Drew-Dickerson dodecamer d(CGCGAATTCGCG)$_2$ in its canonical B form, which was modeled using the stiff Martini DNA forcefield.[35] In both

physiological and endosomal pH, the DNAs were completely deprotonated and the charge on each DNA $Q_{DNA} = -22$. A 586 Da semi-linear PEI with a small degree of branching was used (**Figure 2**),[20] carrying a charge of $Q_{PEI} = 3$ at physiological (referred to as PEI3) and $Q_{PEI} = 6$ at endosomal pH (referred to as PEI6).[20,36] The protonation ratio was based on titration experiments for 600 Da PEIs, which reported 21% protonation at pH = 8 and 47% protonation at pH = 6.[20,36,37] The protonation sites were chosen based on the consideration that primary amines are more prone to protonation and neighboring amines are unlikely to be both protonated. It is assumed that while the protonation state of the PEI is affected by pH, it is not influenced by its binding to the DNAs. The protonated and unprotonated beads were modeled with Q_d and P_1 bead types[23] respectively, based on our previous work[38,39] where the forcefield parameters for the PEI and PEI-DNA interaction were validated[38,39] against AA simulations. The solvent was modeled using the polarizable Martini water[40] with 150 mM of KCl. All simulations were performed in GROMACS 5.[41]

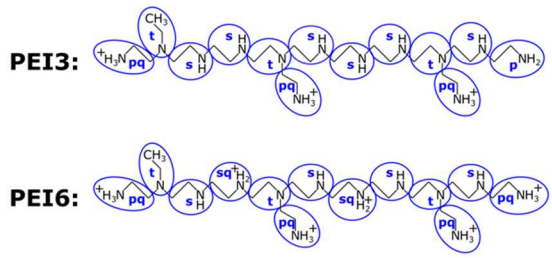

Figure 2. Structures of PEI at physiological (PEI3) and endosomal (PEI6) pH. All-atom (AA) structures are shown in black,[20] whereas the CG structures and mapping scheme are shown in blue. The text in blue represents the type of nitrogen contained in the CG bead, tertiary (t), secondary (s), protonated secondary (sq), primary (p), and protonated primary (pq).

2.1.1 Aggregation Simulations

Four systems with 27 DNAs were simulated, each at a specific pH (physiological or endosomal) and PEI/DNA number ratio ($\alpha = 2$ or 10). The details of these simulated systems are summarized in **Table 1**. The simulations were performed following our previous work[26], but with

a different bead type for unprotonated PEI beads for improved accuracy.[39] All the DNAs were aligned and placed in a 3x3x3 array at the center of a 25 nm cubic box. The closest distance between the centers of mass of DNAs was 6 nm. All the PEIs were placed randomly inside the box, followed by the addition of Martini polarizable water.[40] Appropriate amounts of Martini potassium and chloride ions[23] were added to first neutralize the system and then reach the salt concentration of 150 mM.

Table 1. Details of aggregation and acidification simulations. For aggregation simulations: PEI/DNA number ratio (α), N/P ratio, pH, number of DNAs (N_{DNA}) and PEIs (N_{PEI}), charge of DNA (Q_{DNA}) and PEI (Q_{PEI}), critical α (α_c, calculated from $-Q_{DNA}/Q_{PEI}$) at which the total charge of PEIs and DNAs is zero, total simulations time (t_{sim}). For acidification simulations: acidification rate, and total time to acidify all PEIs (t_{acid}).

Aggregation System	α	**N/P ratio**	**pH**	N_{DNA}	N_{PEI}	Q_{DNA}	Q_{PEI}	α_c	t_{sim} (μs)
P2	2	1.18	Physiological	27	54	-22	3	7.33	9.5
P10	10	5.91	Physiological	27	270	-22	3	7.33	8
E2	2	1.18	Endosomal	27	54	-22	6	3.66	12
E10	10	5.91	Endosomal	27	270	-22	6	3.66	6
Acidification System	α	**N/P ratio**	**Acidification**	N_{DNA}	N_{PEI}	**Acidification rate**		t_{acid} (μs)	t_{sim} (μs)
I2	2	1.18	Instant	27	54	∞		0	13.5
I10	10	5.91	Instant	27	270	∞		0	7
S2	2	1.18	Slow	27	54	1 H^+/ns		0.162	13.5
S10	10	5.91	Slow	27	270	1 H^+/ns		0.810	7

The initial configuration was first energy-minimized using steepest-descent, followed by a constrained NPT simulation for 1 ns and an unconstrained NPT simulation of different times (see t_{sim} in **Table 1**). The length of unconstrained NPT simulations varied based on the time required for a system to reach its steady state, which was defined by observing a stable value for the average NP size $\langle s_{NP} \rangle$ (average number of DNAs in a NP) for 1 μs (see Supporting Information (SI) **Section S1**). For constrained NPT simulations, all the bonds in PEI, DNA backbone, and polarizable Martini water were constrained using LINCS. Van der Waals interaction was cut off at 1.1 nm using the potential-shift-Verlet scheme.[42] Long-range electrostatic interaction was handled by the reaction-field scheme[43] while short-ranged electrostatics was modeled using Coulombic interaction cut off at 1.1 nm.[42] The relative dielectric constant of the solvent and the reaction-field were set to be 2.5 and ∞ respectively.[40] A neighbor list was maintained for the cutoff radius of 1.1

nm using the Verlet scheme[44], which was updated every 20 steps. The pressure was maintained at 1 bar using Berendsen barostat with a time constant of 3 ps and compressibility of 3×10^{-4} bar^{-1}. The temperature was maintained at 300 K using a velocity-rescaling thermostat with a time constant of 0.1 ps. Initial velocities were generated from the Maxwell-Boltzmann distribution for 300 K. A leap-frog integrator was used with a timestep of 5 fs, while applying a periodic boundary condition in all directions. Martini CG-MD simulations do not account for friction between atoms within the same bead, leading to a CG time-scaling by a factor of 3-8.[45] In this work, all simulation time was scaled up by a factor of four (excluding time constants and timestep), a standard factor used to match the self-diffusion coefficient of water in AA and CG simulations.[45] A detailed time-scaling analysis was not performed because the present study does not make direct quantitative comparison of kinetic properties extracted from CG-MD simulations with those from experiments or AA-MD simulations. Unconstrained NPT simulations were similar to the constrained ones, with three differences: (i) initial velocities of the CG beads were assigned from the last step of constrained simulations, (ii) Parrinello-Rahman barostat was used to maintain the pressure at 1 bar, using a time constant of 5 ps and compressibility of 4.5×10^{-5} bar^{-1}, and (iii) constraints were only applied to bonds present in the Martini polarizable water.

2.1.2 Acidification Simulations

The configuration of beads in the last timestep of an aggregation simulation (α = 2 or 10) at physiological pH, i.e., system P2 or P10, was used as the initial configuration for the corresponding acidification simulation. Endosomal acidification was modeled by increasing the protonation of the PEIs from PEI3 to PEI6. This was achieved by modifying three CG beads in PEI3 from P_1 to Q_d (**Figure 2**). Subsequently, an appropriate number of water molecules was replaced, at random, with chloride ions to maintain charge neutrality. Two acidification rates were studied, namely

instant and slow. In instant acidification, all PEIs was changed from PEI3 to PEI6 at the beginning of the simulation. In slow acidification, one PEI was changed from PEI3 to PEI6 every 3 ns, i.e., the acidification rate is 1 H^+/ns. The PEIs were protonated in the order of their molecule ID. Since the PEIs were placed randomly at the beginning of the aggregation simulation, the acidification of PEIs was, in essence, random. The details of these simulations are summarized in **Table 1**.

Unlike the aggregation simulations, only unconstrained NPT simulations were performed, which followed the same settings of unconstrained NPT aggregation simulations (see **Section 2.1.1**). The total simulation time reported in **Table 1** is only for the acidification simulation and does not include the aggregation simulation time. The total simulation time was different for α = 2 and 10, allowing each system to reach steady state where $\langle s_{NP} \rangle$ was not changing significantly for 1 μs (see **SI Section S1**).

2.2 Free Energy Landscape

The free energy of PEI (F) was calculated using Eq 1, where k_B is the Boltzmann's constant, T is the absolute temperature, and P is the probability of finding a PEI with a dimensionless reaction coordinate q at the steady state. The reaction coordinate q for a PEI was defined by Eq 2, where N_{DNA} is the total number of DNAs in the system, d_i is the minimum distance between the PEI and the i^{th} DNA, r_b is a distance that defines binding between PEI and DNA, and H is the Heaviside step function. When a PEI is bound with the i^{th} DNA, $d_i < r_b$ and $H(r_b - d_i)$ is 1. In this case, r_b/d_i is in the range of 1-1.2, where the upper limit of 1.2 arises due to repulsive van der Waals forces. In contrast, if a PEI is not bound to the i^{th} DNA, $d_i > r_b$, $H(d_i - r_b)$ is 1 and r_b/d_i is in the range 0-1. The first term in Eq 2 calculates r_b/d_i for the closest unbound DNA using the max function, and the value ranges between 0 and 1. In the second term in Eq 2, r_b/d_i is summed over all bound DNAs, and the increase in q is in the range of 1-1.2 for every bound DNA. For a free

PEI, q only contains the contribution from the closest unbound DNA, and ranges from 0 to 1. The range of q is 1-2.2 when a PEI is bound to one DNA, since the two terms in Eq 2 contribute values of 0-1 and 1-1.2 respectively. Similarly, the range of q is between k to $1 + 1.2k$ when PEI is bound to k DNAs ($k > 0$). Theoretically there can be some overlap between the ranges of q for a PEI bound to $k - 1$ and k DNAs. However, the overlap observed is minimal. Therefore, in our results the range of q is taken as $1 + 1.2(k - 1)$ to $1 + 1.2k$ when a PEI is bound to k DNAs ($k > 0$; see supporting information (SI) **Section S2**). Consequently, q positively correlates with the number of DNAs the PEI is bound with, hence this continuous variable is a good candidate to be used as the reaction coordinator in the energy landscape. The binding distance r_b was taken as 0.53 nm, the van der Waals' diameter between PEI and DNA beads. The reaction coordinate q was calculated for all PEIs in the system and the range of q was divided into bins of width 0.2 to calculate the probability $P(q)$ required for the free energy calculation in Eq 1. F provides a quantitative measure for the likelihood of PEIs to form simultaneous contact with multiple DNAs.

$$F(q) = -k_B T \ln(P(q)) \tag{1}$$

$$q = \max\left(\frac{r_b}{d_i} H(d_i - r_b)\right) + \sum_{i=1}^{N_{DNA}} \frac{r_b}{d_i} H(r_b - d_i) \tag{2}$$

2.3 *In-silico* fluorescence microscopy

In-silico fluorescence microscopy images were generated using an open source tool previously developed by the authors.[46,47] Briefly, the Gandy point-spread-function[48] (PSF) was used to model a virtual-microscope with the numerical aperture of 1.3, the refractive index of immersion oil and specimen equal to 1.51, and full-width-at-half-maximum (FWHM) scaling factor[46] of 400. The PSF was calculated over a volume of 15x15x25 nm^3 and voxel dimensions of 0.1x0.1x0.2 nm^3, where the third dimension was the optical axis, which is taken to be the z-axis.

The focal plane is taken to be z = 12 nm, near the center of the simulation box. All DNA and PEI particles emitted light of 670 nm (modeling Cy5) and 518 nm (modeling FITC) respectively. For α = 2, the maximum intensities of light emission were 0.1 and 0.5 respectively for DNA and PEI particles; the corresponding values were 0.1 and 0.15 for α = 10. All images were generated by applying the periodic boundary condition in all directions and time-averaging over 50 timesteps, i.e., an effective exposure time of 10 ns. Red and green colors were assigned to DNAs and PEIs respectively, and the colors were mixed based on the color mixing scheme developed by Mahajan and Tang.[46]

2.4 Transition Diagram

As shown in **Error! Reference source not found.a**, a NP structure is graphically presented by a network consisting of nodes (filled circles) that represent DNAs, and edges (lines) connecting the nodes represent the presence of bridging PEI(s) between them. A unique ID was assigned to each NP structure (*e.g.* U_1, U_2, *etc*.). For purposes of explaining the method, nodes corresponding to the same DNA in different NP structures were shown using the same color. Two NP structures were considered to be identical, hence having the same ID, if they had the same nodes and edges.

A transition diagram was created from the IDs of multiple NP structures and arrows indicating the conversions between them. **Error! Reference source not found.b-d** (left) shows some examples, where the number accompanying each arrow stores the time of the transition. A transition diagram illustrates (i) internal restructuring of a NP if one unique ID transitions to another, (ii) NP aggregation if multiple IDs transition into one, (iii) NP dissociation if one ID transitions into multiple, and (iv) exchange of DNAs among several NPs if multiple IDs transition to multiple but different ones. For NP aggregation, arrows were drawn from the aggregating NPs to a '+' symbol, and a separate arrow was drawn from the '+' symbol to the aggregated NP (see

Error! Reference source not found.c, d). Similarly, for NP dissociation and exchange of DNAs among NPs, '–' (see **Error! Reference source not found.c, d**) and '×' (not shown) symbols were used respectively.

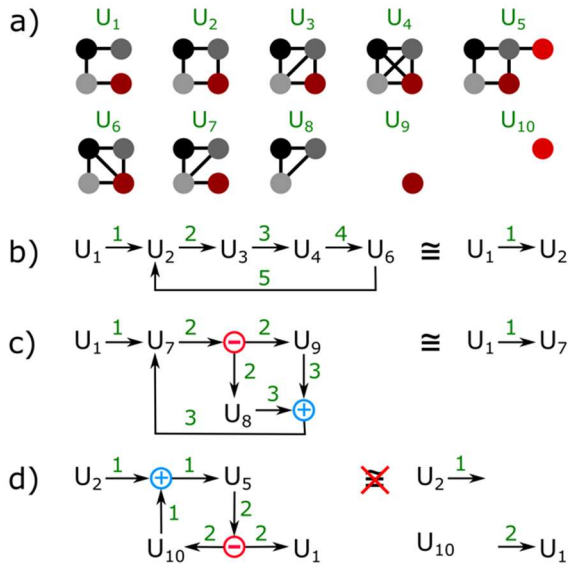

Figure 3. (a) Network representations of NP structures, where nodes are DNAs and edges denote the presence of bridging PEI between a pair of DNAs. Nodes corresponding to the same DNA in different NP structures are shown using the same color. (b), (c) Generation of a principal transition diagram (right) from a complete transition diagram (left) by removing reversible transitions and transition loops. (d) An example where loops cannot be removed from the complete transition diagram (left). Naively removing the loop leads to an unphysical transition diagram (right). In (b)-(d) each number over a directed edge is the time, in nanoseconds, at which the transition occurs.

A principal transition diagram contains the initial and final (at the last timestep) NP structures, as well as transitions between them representing the "net" changes. In some cases, transitions produced IDs already present in the transition diagram. This led to the appearance of a transition loop which was removed to obtain the "net" transitions. For example, the "net" transition was U_1 to U_2 in **Error! Reference source not found.b**, and U_1 to U_7 in **Error! Reference source not found.c**, represented by the principal transition diagrams on the right side of these subfigures. Such loop removal was carried out at each time step when new transitions were added to the transition diagram. Cares were taken for the cases where no transition path was available after the removal to reach the NP structure at the present time step. For example, in **Error! Reference source not found.d,** if the loop U_{10}→'+'→U_5→'–'→U_{10} were removed while keeping the initial

(U_2 and U_{10}) and current IDs (U_1 and U_{10}), there would be no transition path from U_2 to U_1 (**Error! Reference source not found.d**, right), and therefore the loop was kept in the principal transition diagram.

After generating the principal transition diagram, the IDs were replaced with the corresponding NP structures. For each NP structure, the average number of bridging PEIs between each DNA pair was calculated and represented by the thickness of the edge connecting the DNA nodes. The average was performed over the time range when the NP structure was present in the principal transition diagram. The codes for generating the principal and complete transition diagrams have been made available to the public.[49]

2.5 Radius of Gyration

The radius of gyration R_g was calculated using Eq 3, where $r_{i,com}$ is the distance of the i^{th} bead in the NP from its center of mass, m_i is the mass of the i^{th} bead, and N is the total number of beads in the NP. For a NP that crossed a periodic boundary, R_g was calculated after making its structure whole using an open source tool.[49] The average R_g was calculated by root-mean-square averaging.

$$R_g = \left(\frac{1}{N} \sum_{i=1}^{N} m_i r_{i,com}^2 \right)^{1/2} \quad (3)$$

3. Results and Discussion

3.1 Acidic resizing

Four aggregation simulations (see **Section 2.1** for simulation details) were performed, at physiological or endosomal pH, and with α = 2 or 10. α = 2 is less than α_c^e, and α = 10 is greater than α_c^p (**Table 1**). A PEI-DNA pair was considered bound if their minimum distance was below 0.53 nm, the van der Waals diameter between their beads. A NP was defined by a set of PEIs and

DNAs bound together (directly or indirectly through other PEIs and DNAs), and the NP size was quantified by the number of DNAs present in it, s_{NP}. The average NP size $\langle s_{NP} \rangle$ at any time was obtained by directly averaging s_{NP} across all NPs, while the steady state average size $\langle s_{NP} \rangle_{ss}$, (**Figure 4a**) was obtained from the last 1 μs of each simulation (see total simulation time in **Table 1**). As shown in **Figure 4a**, for $\alpha = 2$, $\langle s_{NP} \rangle_{ss}$ is smaller at physiological pH than at endosomal pH, while the result is opposite for $\alpha = 10$. The results support the acidic resizing of NPs proposed in **Figure 1**. Other results of the aggregation simulations are presented in the **SI Section S1**.

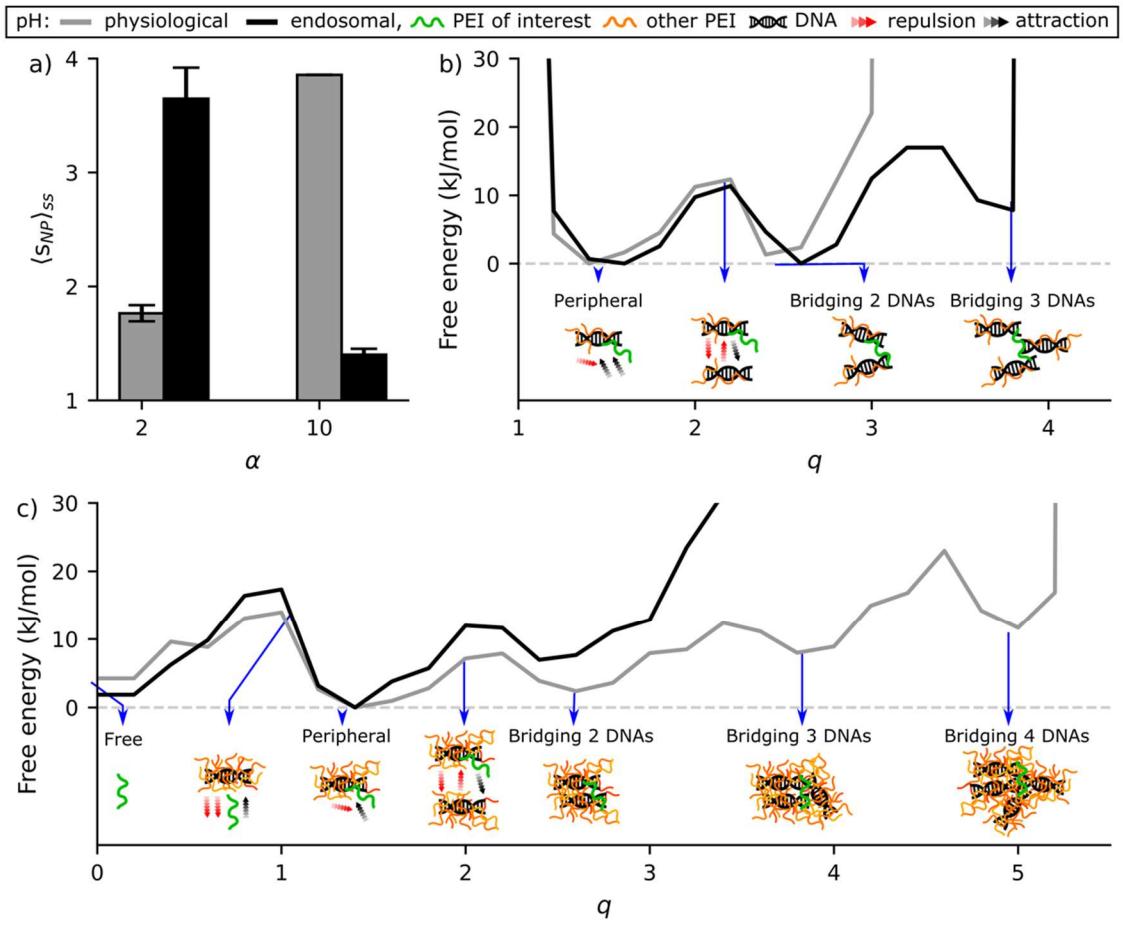

Figure 4. (a) Steady state average NP size ($\langle s_{NP} \rangle_{ss}$) for aggregation simulations at physiological and endosomal pH. Free energy landscape of PEI at physiological and endosomal pH along reaction coordinate q (see Methods **Section 2.2**) for (b) $\alpha = 2$, and (c) $\alpha = 10$ at the steady state. Last 1 μs of each simulation is considered as the steady state (**Table 1**).

To explain the acidic resizing, the free energy landscape of PEI was calculated at the steady state (**Figure 4b**, **c**) along a dimensionless reaction coordinate q (**Section 2.2**) by setting its lowest value to zero (convergence of free energy landscape is provided in **SI Section S3**). q is in the range of: (i) 0-1 when PEI is *free*, i.e., not bound to any DNA, (ii) 1-2.2 when PEI is on the periphery of a NP or *peripheral*, i.e., bound to only one DNA, (iii) 2.2-3.4 when PEI is *2-bridging*, i.e., bridging two DNAs, (iv) 3.4-4.6 when PEI is *3-bridging*, and (v) 4.6-5.8 when PEI is *4-bridging*. The term *bridging PEI* collectively refers to all n-bridging PEIs, where n is an integer greater than 1.

The free energy landscapes in **Figure 4b**, **c** contain local minima representing stable equilibrium states, such as q = 0, 1.5, 2.5, 3.8, and 5 for free, peripheral, 2-bridging, 3-bridging, and 4-bridging PEIs respectively. Two consecutive stable states are separated by a maximum, representing an unstable equilibrium state. Analogous to a reversible chemical reaction, the rate of transition from one stable state to another is regulated by the energy barrier in between. The forward energy barrier associated with increasing q arises due to two repulsive forces. The first is the repulsive force between a PEI and those bound to the DNA it is approaching. This is referred to as *PEI-PEI repulsion* which increases with the number of PEIs (i.e. α) in the system and the degree of protonation. The second is the repulsive force between the DNAs bound to a PEI and the DNA the PEI is approaching. This repulsion is referred to as *DNA-DNA repulsion* and is proportional to the specific repulsion[26] and the number DNAs bound to the PEI (which is n for an n-bridging PEI). The backward energy barrier associated with decreasing q arises due to the attraction between a PEI and the DNA it is approaching, which is referred to as *PEI-DNA attraction* and increases with the degree of protonation of PEI. Conformational changes in the NP can also modulate these attractive and repulsive forces.

For $\alpha = 2$ and physiological pH, the energy barriers at $q = 1.1$ and 3 are very high, denoting the absence of free and 3-bridging PEIs. As pH is decreased from physiological to endosomal condition, PEI-PEI repulsion and PEI-DNA attraction are strengthened due to the increase in PEI charge, and DNA-DNA repulsion is weakened due to the decrease in specific repulsion (DNAs are more neutralized). The strengthening of PEI-PEI repulsion is not significant at such low α. As a result, the energy barrier at $q = 1.1$ remains high, preventing the appearance of free PEIs. Meanwhile, the increased PEI-DNA attraction and reduced DNA-DNA repulsion have lowered the energy barrier at $q = 3$, allowing the formation of stable 3-bridging PEIs and leading to further aggregation of NPs.

For $\alpha = 10$ and physiological pH, there is a large energy barrier at $q = 5.2$, denoting the absence of stable 5-bridging PEIs. Energy barrier near $q = 1$ is not very high and free PEIs are present. Decreasing the pH to endosomal level strengthens PEI-PEI repulsion and PEI-DNA attraction. The DNA-DNA repulsion is also strengthened due to the increase in specific repulsion (DNAs are more over-neutralized). At this large α, the increase of PEI-PEI and DNA-DNA repulsions are significant, causing a large energy barrier to appear at $q = 3.1$. Consequently, the free energy minima at $q = 3.8$ and 5, present for physiological pH, have disappeared for endosomal pH. In addition, while the free energy landscape remains similar for q between 0 and 1.5, at endosomal pH the free energy for $q > 1.5$ is higher than that in physiological pH. All these observations support the conclusion that if the NPs are prepared with $\alpha = 10$, upon endosomal acidification, they tend to dissociate into smaller NPs, with PEIs bridging a smaller number of DNAs and preferring to be peripheral. The acidification simulations allow us to have a closer and more direct look at the resizing of NPs during the acidification process.

3.2 Acidification of NPs prepared with $\alpha = 2$

Endosomal acidification was simulated for two acidification rates, instant and slow (1 H^+/ns). The initial configuration of acidification simulations was taken from the last timestep of the aggregation simulation performed under physiological pH for the same α. The charge of PEIs was increased to model endosomal acidification (see **Section 2.1.2** for details). To facilitate the discussions below, the acidification simulations are referred to as *slow* or *instant acidification simulations*, whereas the aggregation simulations are simply referred to as *physiological* or *endosomal pH simulations*.

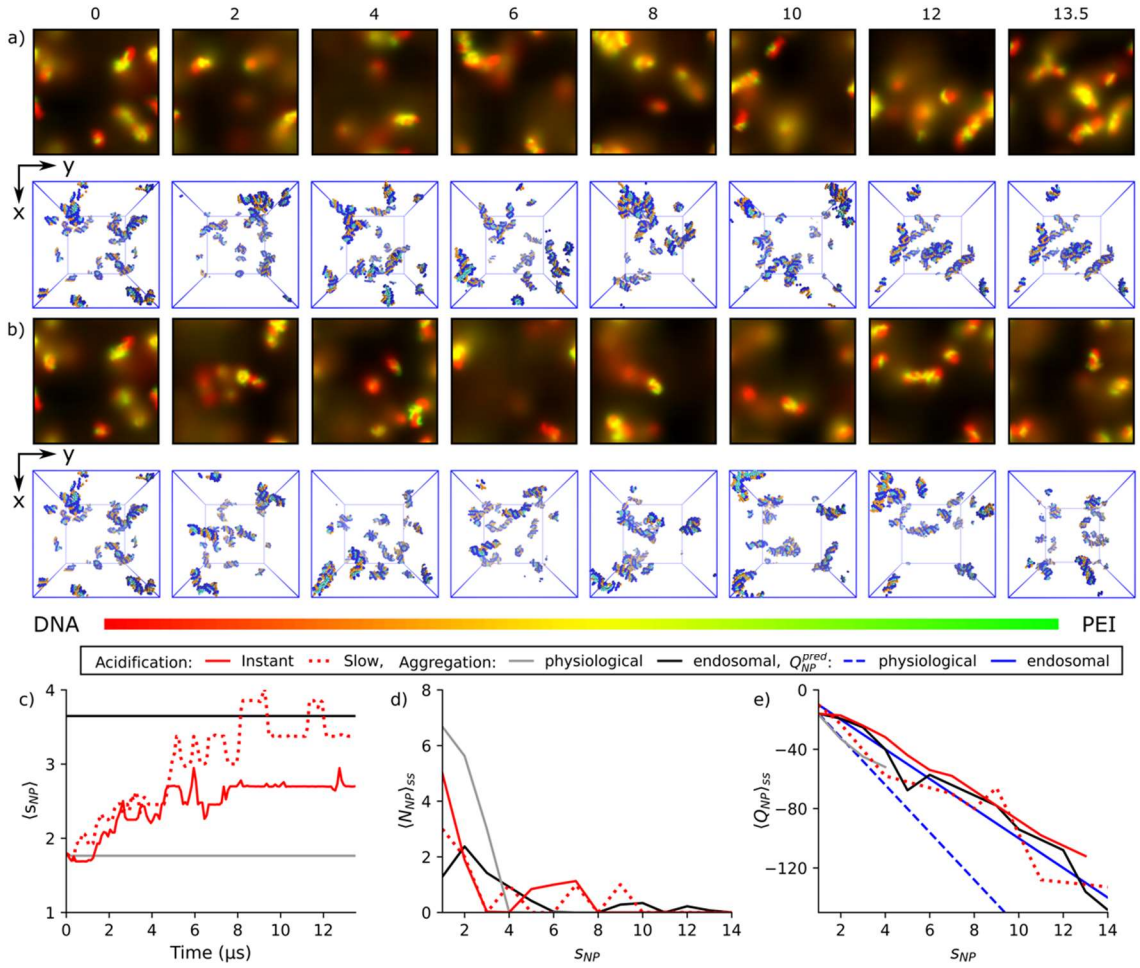

Figure 5. *In-silico* fluorescence microscopy images of (a) instant and (b) slow acidifications, where DNA and PEI emit red and green colors respectively. The colocalization of DNA and PEI produces color between red and green, as shown in the colormap. Simulation time is reported above each image in microseconds. Below each *in-silico* fluorescence image, a corresponding snapshot of the simulation is shown, where PEI beads are orange, DNA backbone

beads are blue, and DNA base beads are cyan. Water and ions are removed for clarity. (c) Time evolution of average NP size $\langle s_{NP} \rangle$ for slow and instant acidification simulations, average performed across all NPs. (d) The steady state number of NPs $\langle N_{NP} \rangle_{ss}$ *vs.* size s_{NP} representing NP size distribution, average performed over time during the steady state. (e) The steady state charge of NPs $\langle Q_{NP} \rangle_{ss}$ *vs.* s_{NP}, averaged across NPs with the same size s_{NP} and over time during the steady state. The predicted NP charge Q_{NP}^{pred} is calculated from steady state of aggregation simulations using Eq 4. The last 1 μs of each simulation is considered as the steady state (**Table 1**). All results are for NPs prepared with $\alpha = 2$.

Figure 5a, b shows the *in-silico* fluorescence microscopy images (**Section 2.3**) of the NPs during acidification, where red and green represent fluorescence of DNA and PEI beads respectively. The color between red and green is produced based on the ratio of DNA and PEI fluorescence, as shown in the colormap. Bright colors indicate particles are in-focus (z = 12 nm), whereas diffused colors indicate they are out-of-focus. Visually examining **Figure 5a**, **b**, larger NPs are observed after 8 μs. Consistent with **Section 3.1**, no free PEI (pure green fluorescence) is observed in the solution. Similar interpretation can be obtained from the simulation snapshots shown below the *in-silico* fluorescence images, as well as quantitatively using the average NP size $\langle s_{NP} \rangle$ (**Figure 5c**). Further aggregation of NPs is observed at both acidification rates as indicated by an increase in $\langle s_{NP} \rangle$ with time. Steady state average size $\langle s_{NP} \rangle_{ss}$ for slow acidification simulation is comparable to that in endosomal pH simulation (shown in black) and higher than that in instant acidification simulation. That is, $\langle s_{NP} \rangle_{ss}$ increases with the decrease in acidification rate.

The steady state number of NPs with size s_{NP}, $\langle N_{NP} \rangle_{ss}$, is plotted against s_{NP} in **Figure 5d**, which describes the steady state size distribution of the NPs. $\langle N_{NP} \rangle_{ss}$ exhibits similar characteristics for both acidification rates, with slow acidification forming larger NPs and instant acidification having more unaggregated DNAs. $\langle N_{NP} \rangle_{ss}$ from endosomal pH simulation is significantly different, forming larger NPs containing as many as 12 DNAs. According to the Smoluchowski coagulation theory, the likelihood of two NPs aggregating together increases with the difference in their size.[26,50] This makes $\langle N_{NP} \rangle_{ss}$ highly dependent on the initial size distribution of NPs in the simulation. Endosomal pH simulation begins with only unaggregated DNAs, which first

aggregates to form a few small NPs (s_{NP} = 2 or 3). These NPs preferentially bind with unaggregated DNAs (s_{NP} = 1) to grow into moderate NPs ($4 \leq s_{NP} \leq 9$). The moderate NPs then preferentially bind with unaggregated DNAs and grow into large NPs ($s_{NP} \geq 10$). The probability of small NPs aggregating with similarly sized small NPs to form stable moderate NPs is low and as a result, in endosomal pH simulation, the NPs tend to be either large or small. The initial size distribution in the acidification simulations is $\langle N_{NP} \rangle_{ss}$ from the physiological pH simulation (**Figure 5d**), with several small NPs and unaggregated DNAs. Upon instant acidification, all the PEIs are protonated at the beginning of the simulation, which decreases the specific repulsions of NPs all at once. As a result, all small NPs compete to bind with unaggregated DNAs and grows simultaneously into moderate NPs. Due to the concurrent competition, it is difficult for moderate NPs to bind with unaggregated DNA in order to grow into large NPs. In slow acidification simulation, the PEIs are protonated sequentially, and therefore the specific repulsion of some NPs decreases earlier. These NPs therefore have the advantage of being able to grow first into larger NPs amid the existing competition. Therefore, the NPs resized during slow acidification are larger than those in instant acidification but smaller than those in endosomal pH simulation.

The steady state charge of NPs with size s_{NP}, $\langle Q_{NP} \rangle_{ss}$, is plotted against s_{NP} in **Figure 5e**. The NP charges at physiological and endosomal pH are predicted (Q_{NP}^{pred}) using Eq 4 and plotted in **Figure 5e**, where Q_{DNA} is the charge of a DNA, Q_{PEI} is the charge of a PEI, and α' is the ratio of the total number of bound PEIs and DNAs.[26] This prediction assumes that all DNAs are bound to an equal number of PEIs. All $\langle Q_{NP} \rangle_{ss}$ decreases with s_{NP} in an almost linear fashion, which agrees with Eq 4. Therefore, each DNA is bound to a similar number of PEIs before and after acidification. Since free PEIs are absent before and after acidification (**Figure 1b**; **Figure 5a**, **b**), it can be concluded that the number of PEIs bound to each DNA remains constant during acidification.

$$Q_{NP}^{pred} = s_{NP}\left(Q_{DNA} + \alpha' Q_{PEI}\right) \quad (4)$$

The above results confirm that NPs prepared at low α further aggregate upon endosomal acidification, and that the acidic resizing hypothesis is valid regardless of the acidification rate. Of more interest is the examination on the acidification of NPs prepared at high α, which according to the hypothesis, can be subjected to dissociation.

3.3 Acidification of NPs prepared with $\alpha = 10$

In-silico fluorescence microscopy images generated for slow and instant acidification of NPs prepared with α = 10 (**Figure 6a, b** respectively) show that green fluorescence in the solution increases with time, indicating that bound PEIs (peripheral or bridging) become free upon acidification. This is further supported by the change in color of NPs from yellow to orange, corresponding to reduced PEI fluorescence in the NPs. Along with the increase in free PEIs, NPs are observed to become smaller, suggesting NP dissociation. Many free PEIs are observed at 0.2 μs in **Figure 6a**, whereas similar density of free PEIs is observed in **Figure 6b** at a later time (1 μs). That is, the release of free PEI from the NPs is faster upon instant acidification than during slow acidification. Similarly, NP dissociation starts at 0.2 μs in **Figure 6a** and later (0.8 μs) in **Figure 6b**. After 3 μs, the difference between the two acidification rates appears minimal. Similarly, the snapshots of simulations shown below the *in-silico* fluorescence images demonstrate the release of PEIs from the NPs. The observations are further quantified by $\langle s_{NP} \rangle$ in **Figure 6c**, where NP dissociation occurs for both acidification rates and is faster under instant acidification. The steady state NP size, $\langle s_{NP} \rangle_{ss}$, is comparable for acidification and endosomal pH simulations. Interestingly, the onset of dissociation in slow acidification simulation, when $\langle s_{NP} \rangle$ starts decreasing, is comparable to the total acidification time of 0.81 μs (**Table 1**). In other words, NP dissociation does not occur until all the PEIs in the system are acidified.

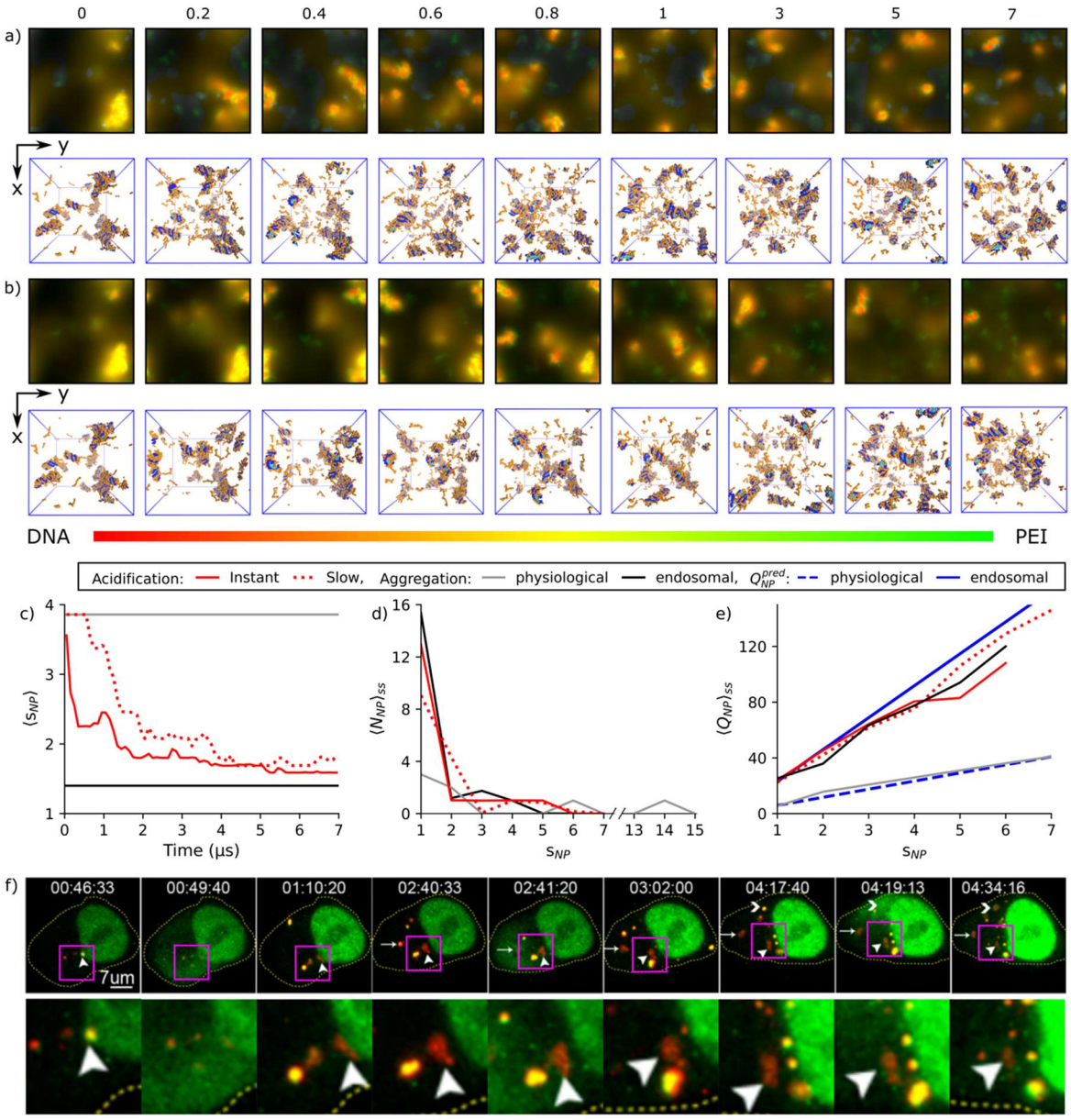

Figure 6. *In-silico* fluorescence microscopy images of (a) instant and (b) slow acidifications, where DNA and PEI emit red and green colors respectively. The colocalization of DNA and PEI produces color between red and green, as shown in the colormap. Simulation time is reported above each image in microseconds. Below each *in-silico* fluorescence image, a corresponding snapshot of the simulation is shown, where PEI beads are orange, DNA backbone beads are blue, and DNA base beads are cyan. Water and ions are removed for clarity. (c) Time evolution of average NP size $\langle s_{NP} \rangle$ for slow and instant acidification simulations, average performed across all NPs. (d) The steady state number of NPs $\langle N_{NP} \rangle_{ss}$ *vs.* size s_{NP} representing NP size distribution, average performed over time during the steady state. (e) The steady state charge of NPs $\langle Q_{NP} \rangle_{ss}$ *vs.* s_{NP}, averaged across NPs with the same size s_{NP} and over time during the steady state. The predicted NP charge Q_{NP}^{pred} is calculated from steady state of aggregation simulations using Eq 4. The last 1 μs of each simulation is considered as the steady state (**Table 1**). All results are for NPs prepared with $\alpha = 10$. (f) Top row: experimental fluorescence microscopy images for PEI-based gene delivery of Cy3-labeled plasmid DNA (red) and FITC-labeled oligonucleotides (green) obtained by Rehman et al.[18] A region of interest is highlighted by adding a pink box in each image, which is magnified and reproduced in the bottom row [Adapted from Rehman et al.[18] Copyright 2013 American Chemical society].

Our results on NP dissociation is consistent with the fluorescence microscopy images of Rehman et al.[18] shown in **Figure 6f**, where 22 kDa linear PEIs (not labeled) are used to deliver Cy3-labeled plasmid DNA (red) and FITC-labeled 17-base pair (ACTACGACCTACGTGAC) oligonucleotide (green) to HeLa cells at the N/P ratio of 5 (yellow representing colocalization of plasmid DNA and oligonucleotide).[18] The red and yellow components of these images, representing the presence of plasmid DNAs, are qualitatively similar to the in-silico fluorescence images in **Figure 6a, b** in that the size of these components reduces over time. Together with the quantitative data in **Figure 6c**, the results suggest that NPs are dissociating in **Figure 6f**, although it was not reported in the original article.[18]

The steady state NP size distribution $\langle N_{NP} \rangle_{ss}$ shown in **Figure 6d**, is similar for acidification and endosomal pH simulations, with slow acidification forming a lower number of unaggregated DNAs (s_{NP} = 1). That is, instant acidification is more efficient in dissociating NPs than slow acidification. This can be explained by a sudden increase in PEI-PEI and DNA-DNA repulsions when the instant acidification is applied, which makes the NPs unstable and prone to dissociation. In contrast, during slow acidification newly protonated PEIs can adjust their conformations and attach to the NPs via local attractions with the DNAs, before other PEIs are protonated. Such conformational changes help reduce repulsive forces within the NPs and delay NP dissociation. Similar to **Figure 5**, the steady state NP charges $\langle Q_{NP} \rangle_{ss}$ in **Figure 6e** scale linearly with s_{NP} and are well predicted by Eq 4. This implies that after acidification, each DNA in the system is bound to a similar number of PEIs. Since bound PEIs are lost during acidification (**Figure 6a**, **b**), the result suggests that each DNA loses a similar number of PEIs to the solution. Understanding how PEIs, especially the bridging ones, are lost is crucial because it controls the structural and geometrical changes of NPs, and hence if and how the NPs dissociate.

3.3.1 Kinetics of bridging PEIs

The numbers of free (N_f/N_{DNA}), peripheral (N_p/N_{DNA}), and bridging (N_b/N_{DNA}) PEIs per DNA, and the average number of bridging PEIs between a pair of bridged DNAs (n_b) are calculated in **Error! Reference source not found.a** as a function of time for both acidification rates (similar analysis for $\alpha = 2$ in **SI Section S4**). Corresponding steady state averages from endosomal pH simulation are shown for reference using horizontal lines. The general trend demonstrates an exponential-like decay for N_b/N_{DNA} and n_b, and a corresponding logistic-like growth in N_f/N_{DNA}. N_p/N_{DNA} remains steady with small fluctuations. The initial change in N_f/N_{DNA}, N_p/N_{DNA}, N_b/N_{DNA} and n_b is faster for instant acidification than for slow acidification, and the difference caused by acidification rate is negligible after 2 μs.

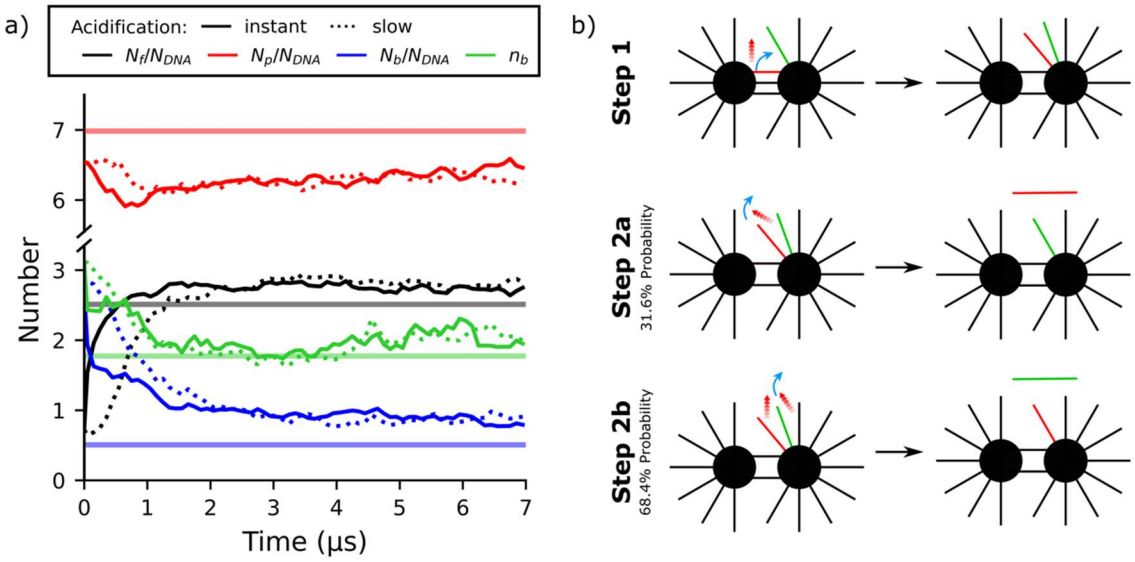

Figure 7. (a) Number of free (black), peripheral (red), and bridging (blue) PEIs per DNA, and the average number of bridging PEIs between a pair of bridged DNAs (green). The horizontal lines represent the steady state averages from endosomal pH simulations. (b) Schematic of transition from bridging to free PEIs. A bridging PEI that is eventually lost is shown in red and a peripheral PEI close to it is shown in green. The blue arrow indicates the transition, and the red arrowheads represent repulsion. All data are from simulations for $\alpha = 10$.

The decay of N_b/N_{DNA} and n_b signifies the loss of bridging PEIs due to acidification, likely caused by increased repulsion between PEIs within the same NP. **Error! Reference source not found.a** shows the stabilization of N_b/N_{DNA} when n_b in the acidification simulations reach the

steady state average in the endosomal pH simulation (at ~3 μs). Because N_b is the product of n_b and the total number of bridged DNA pairs, the results indicate that the number of bridged DNA pairs and the number of bridging PEIs for each DNA pair reach equilibrium at the same time. In turn, this suggests that the primary PEI-PEI repulsion is between bridging PEIs bound to the same DNA pair. The steady state value of N_b/N_{DNA} in the acidification simulations is higher than that in the endosomal pH simulation, which is caused by the higher number of bridged DNA pairs in the acidification simulations. Consistently, $\langle s_{NP} \rangle_{ss}$ is higher in the acidification simulations (**Figure 6c**). During acidification, the free energy landscape of PEIs transitions from the grey curve towards the black curve in **Figure 4c**. Correspondingly, the energy minimum at q = 2.5 (2-bridging PEI) is increased relative to the one at q = 1.5 (peripheral PEI), facilitating the conversion of PEIs from bridging to peripheral. However, as N_b/N_{DNA} and n_b decrease the PEI-PEI and DNA-DNA repulsions reduce, which hinders further increasing of the energy minimum at q = 2.5 and release of the bridging PEIs.

Detailed analysis shows that bridging PEIs convert to peripheral ones and peripheral PEIs convert to free ones (see SI **Section S5**), while maintaining a dynamic balance of N_p/N_{DNA}. At the steady state of the physiological pH simulation, all peripheral PEIs conform to the DNAs so that their repulsions with other bound PEIs are minimized. Upon acidification, as a bridging PEI converts to peripheral, its conformation change tends to increase its repulsion with other bound PEIs, driving it or another peripheral PEI to become free. The increase of N_f/N_{DNA} over time is driven by such transitions. The free energy landscape in **Figure 4c** provides further evidence for such increase. Since acidification reduces the free energy minimum at q = 0 (free PEI) relative to the one at q = 1.5 (peripheral PEI), peripheral PEIs tend to become free and N_f/N_{DNA} would increase.

Error! Reference source not found.b provides a graphical illustration for the typical process of losing a bridging PEI, where DNAs are shown as filled circles and PEIs as straight lines (**Error! Reference source not found.b**). The bridging PEI lost is shown in red, and a nearby peripheral PEI is shown in green. Step 1 shows the transition of the PEI from bridging to peripheral. Two possible scenarios are presented in Step 2a and Step2b for the peripheral to free PEI transition, along with their respective probabilities. In Step 2a, the original bridging PEI becomes free, whereas in Step 2b the neighboring peripheral PEI is freed by PEI-PEI repulsion.

3.3.2 NP structural changes

Structural changes in the NP are illustrated using a *transition diagram*, where each NP structure is represented with a network. The transition diagram can illustrate NP aggregation, dissociation, internal restructuring, as well as exchange of DNAs among multiple NPs (see **Section 2.4** for details). Since the simulations are dynamic, the transition diagrams are complex (SI **Section S6** for α = 2 and 10). Further simplifications are made by removing the loops corresponding to cyclic transitions so that only principal or "net" transitions are retained. This simplified diagram is referred to as the *principal transition diagram* (see **Section 2.4** for details).

Error! Reference source not found. reports the principal transition diagrams for the two largest NPs during instant (**Error! Reference source not found.a, b**) and slow (**Error! Reference source not found.c, d**) acidifications. Diagrams for other NPs at α = 10, and α = 2 are shown in **Section S6**. A black arrow in the diagram indicates the transition between two NP structures, along with the *time of the last transition* (due to the removal of cyclic transitions in between). Each NP structure is comprised of nodes (filled circles) representing the DNAs and edges (lines or curves) between two nodes representing the bridging PEIs. The thickness of each edge is proportional to the number of PEIs bridging the DNA pair, averaged over the period of existence for the NP

structure. An edge is crossed out with a red line if the DNA pair becomes unbridged after a transition, which is referred to as *bridge scission*. An unbridged DNA pair is connected with a blue edge if they become bridged after a transition, which is referred to as *bridge formation*. In the diagram the nodes are arranged to reduce overlapping edges, and the distance between two DNA nodes is not related to their physical separation in the NP. The relative positions of nodes are kept fixed in the same transition diagram to easily identify the DNAs at different simulation time. For example, the DNA marked using red arrows in **Error! Reference source not found.a** is the same DNA at different simulation time. A blue circled plus symbol is used to denote aggregation of two or more NPs, while a red circled minus symbol is used to denote dissociation.

The observed structural changes are similar for both acidification rates and NP sizes. Several bridge scissions occur over time, turning a branched NP structure at 0 μs with many mutually bridged DNAs (especially in **Error! Reference source not found.a**, **c**) into a few linear ones where the DNAs are almost sequentially connected. Almost all bridge scissions are observed for thin edges (except for 1315 ns in **Error! Reference source not found.a**, 52.6 ns in **Error! Reference source not found.b**, and 1472 and 4107 ns in **Error! Reference source not found.d**) with a lower number of bridging PEIs. Generally, the thickness of an edge decreases with time due to the decrease in n_b (**Error! Reference source not found.a**), making it more prone to bridge scission. Two observations can be made for the location of the bridge scissions. First, DNAs that are bridged with several others in a crowded setting are more likely to lose their bridging due to increased DNA-DNA repulsion. The DNA marked with the red arrows in **Error! Reference source not found.a** is bridged with six other DNAs at the beginning of the simulation, making it the most crowded DNA in the NP. Five of these six bridges experience scission at 7.2, 61.2, 105.8 (two bridges), and 1746.4 ns respectively. The only surviving bridge is with the DNA marked by

green arrows, and this pair had the thickest edge among the six at the beginning of the simulation. The same is true for the heavily crowded DNA marked by red arrows in **Error! Reference source not found.c**, which loses all its bridges except the one with the DNA highlighted by green arrows. Second, in NPs having linear structures with minimal mutual association amongst the DNAs, bridge scissions tend to occur near the terminals. A DNA located at the center of such a NP experiences almost equal DNA-DNA repulsion from the two directions, whereas for a DNA near the terminal the repulsive forces would be unbalanced leading to higher probability of bridge scission. For example, the loss of bridged DNA pairs occurs near the terminals at 1315, 1746.4 and 3914.2 ns in **Error! Reference source not found.a**, and at 3001 and 3744.8 ns in **Error! Reference source not found.c**.

Sufficient loss of bridged DNA pairs leads to NP dissociation. In **Error! Reference source not found.a**, the first dissociation occurs at 105.8 ns near the crowded DNA marked with the red arrow. This dissociation forms three linearly structured NPs with s_{NP} = 6, 5 and 3, which further dissociate near their terminals at 1315, 1746.4 and 3914.2 ns respectively, with larger NPs dissociating earlier in time. Similar observations are made in **Error! Reference source not found.b-d**. Terminal DNAs in linearly structured NPs are more prone to dissociation for larger NPs because of they experience stronger unbalanced repulsive force from other DNAs in the same NP. The NP with s_{NP} = 5 in **Error! Reference source not found.a**, created after the dissociation at 1315 ns, undergoes internal restructuring with three bridge formations and two bridge scissions. As a result, a branched NP structure with mutually bridged DNAs is formed, but such restructuring does not seem to be a dominant mode of transition. The final dissociated NPs have similar structures regardless of the acidification rate.

The dissociation mechanisms are highly consistent across the large number of NP structural transitions observed. In the principal transition diagrams (**Error! Reference source not found.** and **Figure S6**), a total of 19 NP dissociations and 46 bridge scissions are observed, all following similar mechanisms. Furthermore, the principal transition diagrams include 37 and 42 structures for instant and slow acidification respectively, whereas the transition diagrams explore 131 and 223 structures respectively (**Table S3**). Therefore, the influence of NP structure on its evolution and transition mechanisms is well represented.

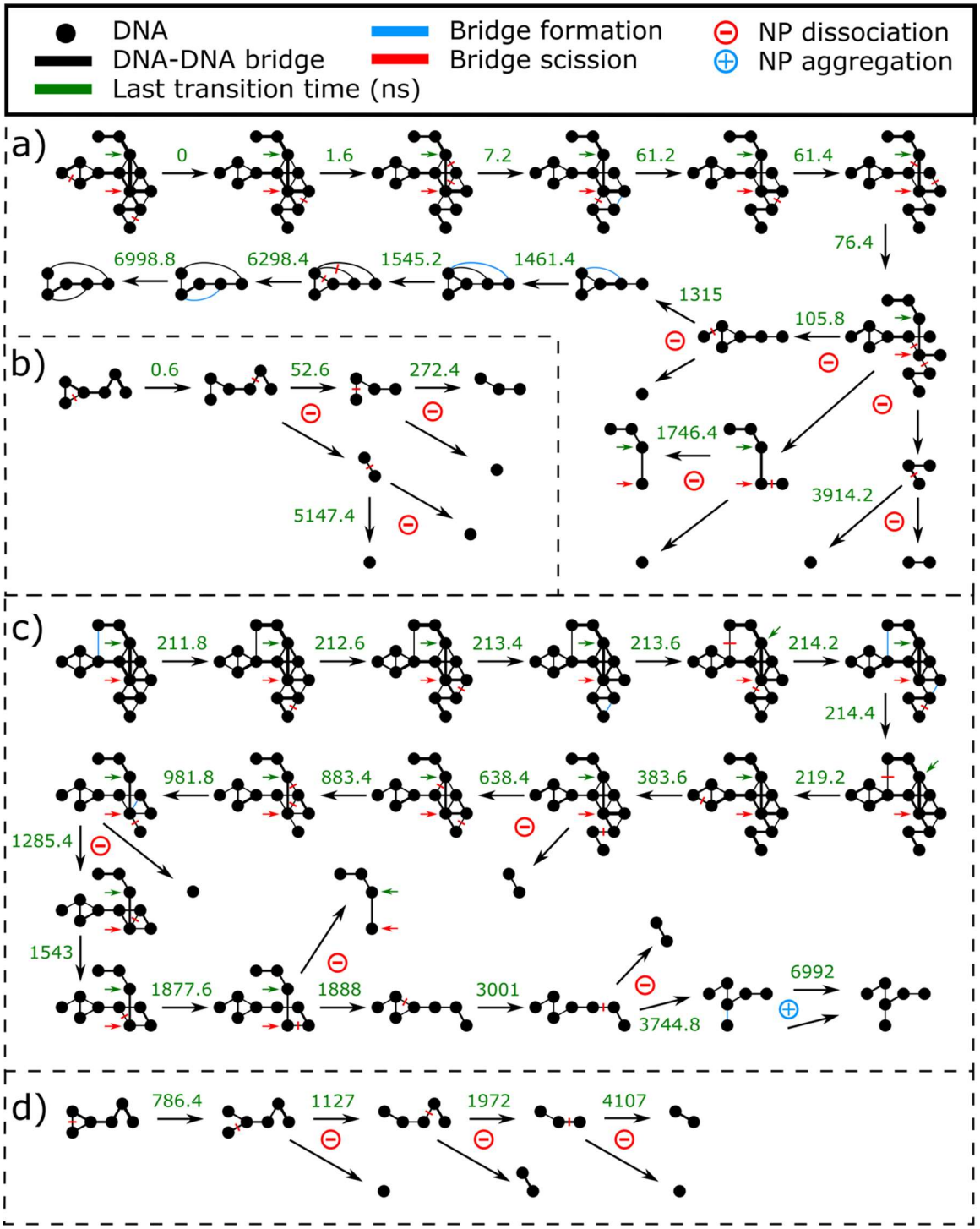

Figure 8. Principal transition diagrams of NPs in acidification simulations for α = 10. (a) Largest and (b) second-largest NP in the instant acidification simulation. (c) Largest and (d) second-largest NP in the slow acidification simulation.

The greatest difference found in NP dissociation upon slow and instant acidifications is the onset of the principal transition. Under instant acidification, the first principal transition occurs at

0 ns (**Error! Reference source not found.a**), whereas under slow acidification it occurs at 211.8 ns (**Error! Reference source not found.c**). Prior to 211.8 ns, several transition loops are observed (see SI **Section S6**) suggesting that the loss of bridged DNA pairs is more reversible under slow acidification than that under instant acidification. Such reversibility can also be seen in **Error! Reference source not found.c**: a bridged DNA pair is formed at 211.8 ns, lost at 214.2 ns, reformed at 214.4 ns, and lost again at 219.2 ns. This higher reversibility delays NP dissociation under the slow acidification condition.

2.3.3 NP swelling and shrinkage

The radius of gyration averaged across all NPs, $\langle R_g \rangle$, (see **Section 2.5**) is shown in **Figure 9a** for the two acidification simulations. The steady state average radii of gyration evaluated from physiological and endosomal pH simulations are shown using light-grey and dark-grey horizontal lines respectively. The overall decreasing trend in $\langle R_g \rangle$ is consistent with $\langle s_{NP} \rangle$ (**Figure 6c**) and therefore mainly due to dissociation of NPs. When NPs are not dissociating, their radius of gyration (R_g) can increase (corresponding to NP swelling), decrease (corresponding to NP shrinkage), or remain steady. To explore this, R_g for the largest and second-largest NP, before their dissociation, is shown in **Figure 9b, c** respectively. The light-grey horizontal line in each subfigure represents the NP's steady state average R_g from the physiological pH simulation. Since the time at which the NPs dissociate is different in slow and instant acidifications, time on the horizontal axis of **Figure 9b, c** is reported as the percentage of the total lifetime of the undissociated NPs.

In **Figure 9b,** an overall increase in R_g is observed for both acidification simulations, i.e., NP swells. This swelling can be explained by the bridge scissions that occur in the NPs (0-105.8 ns in **Error! Reference source not found.a**; 0-638.4 ns in **Error! Reference source not found.c**) and subsequent increase in DNA-DNA distance. The snapshots of the largest NP are shown in

Figure 9b as insets: grey for $t = 0$, black for just before dissociation under instant acidification, and red for just before dissociation under slow acidification. Swelling of the NPs is visually detected, where "arms" containing DNA and PEI beads extend outwards from the NP's center after their acidification.

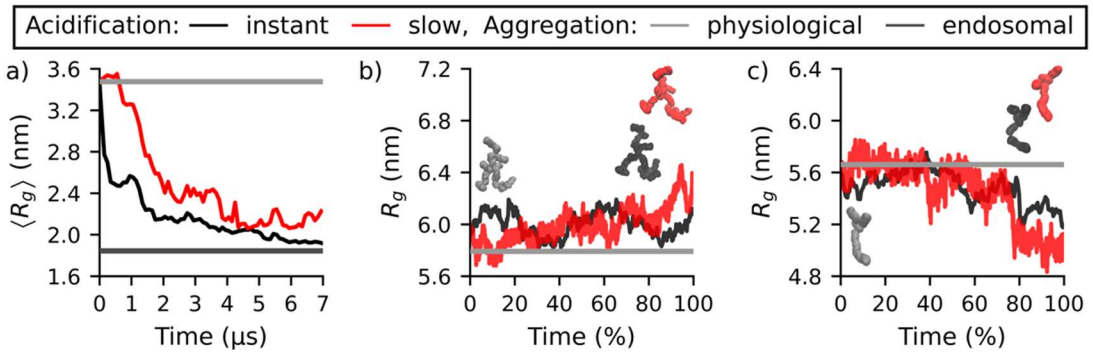

Figure 9. (a) Average radius of gyration $\langle R_g \rangle$ as a function of time. Radius of gyration of the (b) largest NP with s_{NP} = 14, and (c) second-largest NP with s_{NP} = 6 before dissociation. In (b, c), snapshots of the NPs are shown in grey at $t = 0$, and in black (instant acidification) or red (slow acidification) at the onset of dissociation.

In **Figure 9c**, R_g decreases over time for both acidification simulations, i.e., NP shrinks. Similar to **Figure 9b**, the snapshots of the second-largest NP are shown in grey at $t = 0$, and black (instant acidification) or red (slow acidification) at the onset of dissociation. Different from the largest NP shown in **Figure 9b**, the second-largest NP has a more linear, rod-like structure. Under instant acidification, the NP shrinkage is produced by the bending of the rod-like structure, whereas under slow acidification it occurs due to a DNA moving to the center of the NP after a bridge scission (786.4 ns in **Error! Reference source not found.d**; t = 70%). NP swelling and shrinkage are therefore dependent on the initial NP geometry, structure and the internal restructuring that take place upon acidification.

3.4 Implication to gene delivery

Endosomal acidification is found to cause a resizing of NPs, which strongly depends on the N/P ratio at which they are prepared. At physiological pH, NPs prepared with a low N/P ratio (1.18; $\alpha = 2$) has a small average size (in terms of the number of DNAs present in the NPs) and no free

PEIs are found in the solution (**Section 3.1**). Upon endosomal acidification, the average NP size increases (**Figure 5c**) and the number of free PEIs remains zero (**Section 3.1**). Increase in NP size indicates further aggregation of small NPs into larger ones. On the contrary, under physiological pH NPs prepared with a high N/P ratio (5.91; α = 10) has a larger average size with free PEIs in the solution (**Section 3.1**). Upon endosomal acidification, the average NP size decreases (**Figure 6c**) and the number of free PEIs in the solution increases (**Error! Reference source not found.a**), suggesting the dissociation of large NPs into smaller ones. The term "dissociation" here may not imply complete separation of DNAs from the PEIs as it was used in some literature [31,51], although some PEIs are freed during the process. Similar to our results, Rehman *et al.*[18] observed dissociation of NPs within the endosome of HeLa cells, where the NPs were prepared at N/P ratio of 5 using 22 kDa linear PEIs along with plasmid DNA and 17-base pair oligonucleotides (**Figure 6f**). This is comparable with our study using N/P ratio of 5.91 and 12-base pair DNAs, although the 586 Da PEI in this work is much smaller.

Acidic resizing of NPs has strong implications in the endosomal escape and nuclear trafficking of DNAs. Several mechanisms have been proposed in the literature for PEI-facilitated endosomal escape. First, based on the "proton sponge" hypothesis,[13,16] the osmotic pressure of the endosome can increase with the number of PEIs in it, due to the entry of water and counterions caused by PEIs' protonation. Second, endosomal acidification of free PEIs can also increase the osmotic pressure, even without the entry of water and counterions, based on the theoretical study of Yang and May[29]. This is supported by several experimental studies, such as in CT26 and 293T cells, where the presence of free PEIs in the endosome increased the efficacy of gene delivery.[52,53] Third, oncotic pressure or colloidal osmotic pressure in the endosome can increase with a rise in the number of free PEIs. This effect has been reported for non-viral carriers such as lactosylated

poly(ethylene glycol)[54,55] in Hepatoma cells but not for PEIs. Increase in osmotic pressure can lead to endosomal swelling and its subsequent rupture or burst. Finally, PEIs can damage the endosomal membrane and the membrane damaging capability correlates positively with the number of PEIs in the endosome.[10,19] Results in the present work suggests that PEI-induced endosomal escape might depend on the N/P ratio at which the NPs were prepared. At high N/P ratio, the number of PEIs is large and free PEIs are present which may increase upon endosomal acidification. Furthermore, NP dissociation could occur, increasing the number of NPs in the endosome. These effects both have the potential to increase the osmotic pressure and facilitate membrane damage, thus enhancing endosomal escape. In contrast, at a low N/P ratio, the number of PEIs is small, and it is less likely to have free PEIs even after endosomal acidification. In fact, endosomal acidification could result in further aggregation of NPs which would then reduce the colloidal osmotic pressure. Consequently, osmotic pressure and membrane damage may be decreased leading to low endosomal escape. It is interesting to note that low transfection efficacy was reported in lung of mice[56] and Raw264 cells[5] for N/P ratio of 1, as compared to high transfection efficacy in COS-7 and CHO-K1 cells for N/P ratio of 6.[57] These observations are consistent with implications from our simulations, despite the difference in time and length scales.

After the endosomal escape, NPs are released into the cytoplasm, where bound PEIs protect the DNAs from degradation.[3] As the pH rises to cytosolic pH (6.9-7.4),[58] PEIs could get deprotonated which in turn can affect PEI-DNA interactions and sizes of the NPs. For example, dissociated NPs could aggregate again due to reduced PEI-PEI repulsion, which could be hindered by the more voluminous cytoplasm that promotes NP dispersion.[18] From experiments, there has not been consensus regarding whether complete dissociation of DNAs from the PEIs is necessary for successful transfection. Some reported that DNAs and PEIs never fully separated in cells such

as EA.hy 926, COS-7, and CFPAC-1,[6,34] while others argued that complete separation was vital for gene delivery[18,31,51] in cells such as 293T and HeLa. Simulations results in this work suggest that regardless of the N/P ratio at which the NPs are prepared, complete separation of PEIs from DNAs is unlikely. That is, the presence of molecules that has more binding affinity to DNA than PEI might be necessary for complete dissociation. It has been reported that nuclear trafficking of NPs can occur passively through diffusion if their diameter is less than 9 nm, or actively via short amino acid sequences and nuclear transport proteins if their diameter is between 9 and 39 nm;[59–61] NPs with diameter more than 39 nm cannot be trafficked.[59,60] Since the diameter of NPs prepared for gene delivery is on the order of 100 nm,[18,57] their dissociation into smaller NPs appears essential, which has been observed in our simulations for NPs prepared with a high N/P ratio. Our simulations suggests that endosomal escape of NPs prepared at low N/P ratio would be inferior, because DNAs are not well protected by PEIs (red colored regions in **Figure 5a**) and could be digested in the endo-lysosomal compartment. If such NPs are able to successfully escape from the endosome, nuclear trafficking should not be of significant concern because the NPs would likely dissociate as the pH rises; however, the poorly protected DNAs might still be subject to enzymic degradation in the cytoplasm. Pollard *et al*.[6] reported poor transfection efficacy of NPs prepared with N/P ratio of 4.2 (1 charge equivalent) when injected into the cytoplasm of COS-7 cells, which could be due to the degradation of DNAs.

The rate of endosomal acidification can affect the acidic resizing of NPs, and it depends on the number of proton pumps in the endosome and the available chemical energy (adenosine-triphosphate; ATP). The actual endosomal acidification rate is expected to be on the order of 10^{-7} H^+/ns,[62] but such a low rate is not accessible by simulations due to the current computational limit. Two acidification rates, instant and slow (1 H^+/ns), are simulated in this work to qualitative assess

its effect. The results suggest a limited influence of acidification rate on the overall dissociation of NPs prepared with high N/P ratio, and thereby on their endosomal escape and nuclear trafficking. For the NPs prepared with a low N/P ratio, slow acidification produces larger NPs. It is therefore reasonable to suspect that at an acidification rate of 10^{-7} H^+/ns, the average NP size could be even larger, further reducing the probability of endosomal escape.

To increase the efficacy of PEI-based gene delivery with a high N/P ratio, it is desirable to enhance the NP dissociation upon endosomal acidification, which would translate to higher efficacy of endosomal escape and nuclear trafficking. There is a remarkable consistency in the dissociation mechanisms at both acidification rates such as, loss of bridging PEIs due to repulsion from PEIs bound to the same DNA, bridge scission between DNA pairs with a low number of bridging PEIs, NP dissociation near crowded DNAs due to DNA-DNA repulsion, *etc*. We can exploit these mechanisms to design PEIs that can potentially promote NP dissociation during acidification. Specifically, the following targets are proposed for NP preparation: reducing DNA-DNA separation, promoting DNA crowding (increasing mutual bridging of DNAs), and forming NPs with a moderate number of bridging PEIs. We suspect a PEI with moderate molecular weight (MW) and degree of branching would be an effective candidate. If the MW of the PEI is too low, it might hinder the formation of large NPs that can later dissociate, whereas if the MW is too high the DNAs might be far apart causing difficulties in NP dissociation due to low DNA-DNA repulsion. High transfection efficacy has been reported for PEI with moderate[63] (12 kDa better than 1616 kDa in K5 Cells) and high[64] (70 kDa better than 10 kDa and 2 kDa in EA.hy 926 cells) MW. However, these results are reported for polydisperse PEIs and are not informative of the optimal MW of PEIs. Werth *et al.*[65] fractionated commercially available polydisperse 25 kDa PEIs and found moderate MW PEIs (4-10 kDa) had the highest transfection efficacy in SKOV-3 cells,

with undetectable transfection efficacy of PEIs above 10 kDa and below 2 kDa. Bieber *et al*.[66] fractionated the same PEIs and found those with MW in the range of 0.5-10 kDa had the highest transfection efficacy in PaTu 8902 cells. These results are consistent and align with the hypothesis that moderate MW PEIs are likely more efficacious. If a PEI has a dendritic structure, it could crowd several DNAs, but the number of bridging PEIs would be low and hence their repulsion, making NP dissociation difficult. While linear PEIs could create a large number of bridging PEIs, bridge scission upon endosomal acidification could be inadequate. Comparison of transfection efficacy between linear and branched PEIs has been reported to differ between cell lines and between *in-vitro* and *in-vivo*.[57,67] To the best of our knowledge, the only study that systematically explored the effect of the degree of branching of the PEI (measured using ^{13}C NMR spectroscopy) on the transfection efficacy was conducted by Krämer *et al*.[68] Consistent with our supposition, the transfection efficacy was found to be highest for the degree of branching of 58% (among 0, 58, 72, and 100%) for NIH/3T3 and COS-7 cells. Further investigation on the combined effect of degree of branching and MW on transfection efficacy in different cell lines is needed to ascertain the optimal PEI properties for gene delivery, by performing simulations with high molecular weight PEI with different degrees of branching.

3.5 Limitations

The aggregation or dissociation of NPs presented here are likely to be applicable for double stranded short nucleotides such as short-interfering RNAs and oligonucleotides. Large nucleotides may follow similar mechanisms for NP structural transitions, but a few differences can be expected. If we consider the 12-base pair DNAs in this work as fragments of a larger DNA, complete bridge scission between two large DNAs will only take place if bridge scission occurs for all the fragments, which is more difficult. Large NPs were observed to swell before dissociation (**Figure 9**), which

leads to the expectation that NPs containing large DNAs would swell significantly upon acidification. This is consistent with the reported decondensation of plasmid DNAs.[18] Additional phenomena such as bending of large DNAs can affect its decondensation or dissociation, which require further investigation.

The protonation states of PEIs are expected to be affected not only by the global ambient pH, but also by their local environment such as the surrounding DNA beads. In this study the protonation states of PEIs were preassigned based on titration experiments at pH = 6 and 8,[36] while potential variation of protonation with local environment was not considered. Such an approach has been adopted by existing AA- and CG-MD studies in the literature on DNA-polycation complexation and aggregation.[20,22,25,69,70] A more accurate approach would be to model dynamic protonation and deprotonation, which could be achieved by the titratable Martini 3.0 forcefield[71] or MD coupled with Monte-Carlo techniques.[72] Such methods are beyond the scope of this work because the DNA and PEI forcefield here (developed for Martini 2.0) needs further development to make it compatible with Martini 3.0.

Counter-ion release has been reported in AA-MD simulations to play a role during aggregation of macromolecules.[73,74] Such an effect was not found to be substantial in our simulations (see **SI section S8**). To our knowledge, effects of counterion release are not discussed for Martini CG simulations. One possible reason could be that Martini ions are modeled with its first hydration shell,[75] which cannot capture the direct interactions between ion and macromolecule. For example, in our previous study, Martini ions could not capture the first peak in the radial distribution function between protonated amines of PEI and chloride ions that was observed in AA simulations.[38] Therefore, reduced counter-ion release may be a limitation of the Martini ion. Polarizable Martini ions[76] can be used in future studies to improve electrostatics and ion transport

in concentrated salt solutions, however, significant improvement in counterion release is not expected because ions are still modeled with its hydration shell.

Although experimentally endosomal escape typically occurs at 310 K, CG-MD simulations in this study were performed at 300 K because the PEI-DNA interactions were validated at the same temperature.[38,77] A difference of 10 K is unlikely to produce qualitatively different results because the thermal energy only differs by 0.08 kJ/mol, whereas the potential of mean force associated with PEI-DNA binding is over two orders of magnitude higher (around 30 kJ/mol).[22,38,77] It is worth noting that some gene delivery experiments have been performed at lower temperatures, such as 300 K used in this work.[78,79] We recognize that larger timesteps (20 fs and above) have been used in some Martini CG-MD simulations,[40,75] however, a small timestep of 5 fs was needed to account for instabilities associated with polarizable Martini water in a large system. Specifically, a polarizable water bead could be trapped in an unrealistic configuration between PEI or DNA beads, which can be avoided using a smaller timestep. Similar timestep has been reported in other works.[28] Finally, a factor of 4 was used for the CG time-scaling, a standard approach widely used for Martini CG simulations.[24] A detailed analysis would be needed to determine an accurate value for this factor if kinetic properties as the diffusion coefficient were to be predicted for comparison with experiments. Quantitative evaluation of these kinetic properties is not the focus of the present work. While the CG time should be interpreted with care, a detailed time-scaling analysis is not deemed necessary for this work as the scaling factor is expected to be similar for all systems simulated and compared here.

4. Conclusions

Large-scale coarse-grained simulations are performed to study the size and structural changes of PEI/DNA NPs when subjected to endosomal acidification. The results reveal an acidic

resizing of NPs that is highly dependent on the N/P ratio at which they are prepared. NPs prepared with a low N/P ratio at physiological pH aggregate further upon acidification, whereas those prepared with a high N/P ratio dissociate. The extent of NP aggregation is sensitive to the rate of acidification, with more aggregation occurring under slow acidification (1 H^+/ns) as compared to instant acidification. However, acidification rate has limited influence on the overall dissociation of NPs prepared with high N/P ratio, and the main consequence of a slower acidification is a delay in the onset of NP dissociation.

During endosomal acidification of NPs prepared at high N/P ratio, some PEIs bound to DNAs are released into the solution due to the repulsion between PEIs bridging the same DNA pair. Reduction in the number of bridging PEIs leads to bridge scission, i.e., disconnection, between some DNA pairs, making the NP more prone to dissociation. Bridge scission is more likely to occur near DNAs that are crowded (bridged to several other DNAs), and near the terminals of a NP with a linear structure. Principal transition diagrams are created to illustrate the structural changes of the NPs during acidification, and free energy landscapes of the PEIs facilitate the understanding of the forces (PEI-PEI repulsion, DNA-DNA repulsion, PEI-DNA attraction) driving those structural changes.

Supporting Information: Relation between reaction coordinate q and PEI state, additional results for physiological and endosomal pH simulation, kinetics of bridging PEIs for α = 2, transition between PEIs, transition diagram, principal transition diagram.

Author Information: Corresponding Author: tian.tang@ualberta.ca

Acknowledgments: We acknowledge the computing resources and technical support from Western Canada Research Grid (WestGrid). T. T. acknowledges financial support from the Natural Sciences and Engineering Research Council (NSERC) of Canada. S. M. is grateful for the Sadler

Graduate Scholarship, Alberta Graduate Excellence Scholarship, R. R. Gilpin Memorial Scholarship, and Mitacs Globalink Graduate Fellowship.

Data and Code availability: https://github.com/subhamoymahajan/NPanalysis version v.1.3. https://github.com/subhamoymahajan/in-silico-microscopy v.1.2.2.

References

(1) Verma, I. M.; Somia, N. Gene Therapy - Promises, Problems and Prospects. *Nature* **1997**, *389* (6648), 239–242.

(2) Lungwitz, U.; Breunig, M.; Blunk, T.; Göpferich, A. Polyethylenimine-Based Non-Viral Gene Delivery Systems. *Eur. J. Pharm. Biopharm.* **2005**, *60* (2), 247–266.

(3) Godbey, W. T.; Barry, M. A.; Saggau, P.; Wu, K. K.; Mikos, A. G. Poly(Ethylenimine)-Mediated Transfection: A New Paradigm for Gene Delivery. *J. Biomed. Mater. Res.* **2000**, *51* (3), 321–328.

(4) Khalil, I. A.; Kogure, K.; Akita, H.; Harashima, H. Uptake Pathways and Subsequent Intracellular Trafficking in Nonviral Gene Delivery. *Pharmacol. Rev.* **2006**, *58* (1), 32–45.

(5) Oh, Y.-K.; Suh, D.; Kim, J. M.; Choi, H.-G.; Shin, K.; Ko, J. J. Polyethylenimine-Mediated Cellular Uptake, Nucleus Trafficking and Expression of Cytokine Plasmid DNA. *Gene Ther.* **2002**, *9* (23), 1627–1632.

(6) Pollard, H.; Remy, J. S.; Loussouarn, G.; Demolombe, S.; Behr, J. P.; Escande, D. Polyethylenimine but Not Cationic Lipids Promotes Transgene Delivery to the Nucleus in Mammalian Cells. *J. Biol. Chem.* **1998**, *273* (13), 7507–7511.

(7) Kay, M. A.; Glorioso, J. C.; Naldini, L. M. Viral Vectors for Gene Therapy: The Art of Turning Infectious Agents Into Vehicles of Therapeutics. *Nat. Med.* **2001**, *7* (1), 33–40.

(8) Glover, D. J.; Lipps, H. J.; Jans, D. A. Towards Safe, Non-Viral Therapeutic Gene Expression in Humans. *Nat. Rev. Genet.* **2005**, *6*, 299–310.

(9) Yin, H.; Kanasty, R. L.; Eltoukhy, A. A.; Vegas, A. J.; Dorkin, J. R.; Anderson, D. G. Non-Viral Vectors for Gene-Based Therapy. *Nat. Rev. Genet.* **2014**, *15* (8), 541–555.

(10) Bieber, T.; Meissner, W.; Kostin, S.; Niemann, A.; Elsasser, H.-P. Intracellular Route and Transcriptional Competence of Polyethylenimine-DNA Complexes. *J. Control. Release* **2002**, *82*, 441–454.

(11) Godbey, W. T.; Wu, K. K.; Mikos, A. G. Poly(Ethylenimine)-Mediated Gene Delivery Affects Endothelial Cell Function and Viability. *Biomaterials* **2001**, *22*, 471–480.

(12) Akinc, A.; Thomas, M.; Klibanov, A. M.; Langer, R. Exploring Polyethylenimine-Mediated DNA Transfection and the Proton Sponge Hypothesis. *J. Gene Med.* **2005**, *7* (5), 657–663.

(13) Behr, J.-P. The Proton Sponge: A Trick to Enter Cells the Viruses Did Not Exploit. *Chimia (Aarau).* **1997**, *51* (1–2), 34–36.

(14) Boussif, O.; Lezoualc'h, F.; Zanta, M. A.; Mergny, M. D.; Scherman, D.; Demeneix, B.; Behr, J. P. A Versatile Vector for Gene and Oligonucleotide Transfer into Cells in Culture and In Vivo: Polyethylenimine. *Proc. Natl. Acad. Sci. U. S. A.* **1995**, *92* (16), 7297–7301.

(15) Monnery, B. D. Polycation-Mediated Transfection: Mechanisms of Internalization and Intracellular Trafficking. *Biomacromolecules* **2021**, *22* (10), 4060–4083.

(16) Sonawane, N. D.; Szoka, F. C.; Verkman, A. S. Chloride Accumulation and Swelling in

Endosomes Enhances DNA Transfer by Polyamine-DNA Polyplexes. *J. Biol. Chem.* **2003**, *278* (45), 44826–44831.
(17) Vermeulen, L. M. P.; Brans, T.; Samal, S. K.; Dubruel, P.; Demeester, J.; De Smedt, S. C.; Remaut, K.; Braeckmans, K. Endosomal Size and Membrane Leakiness Influence Proton Sponge-Based Rupture of Endosomal Vesicles. *ACS Nano* **2018**, *12* (3), 2332–2345.
(18) Rehman, Z. U.; Hoekstra, D.; Zuhorn, I. S. Mechanism of Polyplex- and Lipoplex-Mediated Delivery of Nucleic Acids: Real-Time Visualization of Transient Membrane Destabilization Without Endosomal Lysis. *ACS Nano* **2013**, *7* (5), 3767–3777.
(19) Klemm, A. R.; Young, D.; Lloyd, J. B. Effects of Polyethyleneimine on Endocytosis and Lysosome Stability. *Biochem. Pharmacol.* **1998**, *56* (1), 41–46.
(20) Sun, C.; Tang, T.; Uludağ, H.; Cuervo, J. E. Molecular Dynamics Simulations of DNA/PEI Complexes: Effect of PEI Branching and Protonation State. *Biophys. J.* **2011**, *100* (11), 2754–2763.
(21) Ziebarth, J.; Wang, Y. Molecular Dynamics Simulations of DNA-Polycation Complex Formation. *Biophys. J.* **2009**, *97* (7), 1971–1983.
(22) Bagai, S.; Sun, C.; Tang, T. Potential of Mean Force of Polyethylenimine-Mediated DNA Attraction. *J. Phys. Chem. B* **2013**, *117* (1), 49–56.
(23) Marrink, S. J.; Risselada, H. J.; Yefimov, S.; Tieleman, D. P.; de Vries, A. H. The MARTINI Force Field: Coarse Grained Model for Biomolecular Simulations. *J. Phys. Chem. B* **2007**, *111* (27), 7812–7824.
(24) Marrink, S. J.; Tieleman, D. P. Perspective on the Martini Model. *Chem. Soc. Rev.* **2013**, *42* (16), 6801–6822.
(25) Wei, Z.; Luijten, E. Systematic Coarse-Grained Modeling of Complexation Between Small Interfering RNA and Polycations. *J. Chem. Phys.* **2015**, *143* (24), 243146.
(26) Mahajan, S.; Tang, T. Polyethylenimine-DNA Ratio Strongly Affects Their Nanoparticle Formation: A Large-Scale Coarse-Grained Molecular Dynamics Study. *J. Phys. Chem. B* **2019**, *123* (45), 9629–9640.
(27) Tian, W. De; Ma, Y. Q. Insights into the Endosomal Escape Mechanism via Investigation of Dendrimer-Membrane Interactions. *Soft Matter* **2012**, *8* (23), 6378–6384. https://doi.org/10.1039/c2sm25538c.
(28) Bruininks, B. M. H.; Souza, P. C. T.; Ingolfsson, H.; Marrink, S. J. A Molecular View on the Escape of Lipoplexed Dna from the Endosome. *Elife* **2020**, *9*, 1–16. https://doi.org/10.7554/eLife.52012.
(29) Yang, S.; May, S. Release of Cationic Polymer-DNA Complexes From the Endosome: A Theoretical Investigation of the Proton Sponge Hypothesis. *J. Chem. Phys.* **2008**, *129* (18), 185105.
(30) Freeman, E. C.; Weiland, L. M.; Meng, W. S. Modeling the Proton Sponge Hypothesis: Examining Proton Sponge Effectiveness for Enhancing Intracellular Gene Delivery Through Multiscale Modeling. *J. Biomater. Sci. Polym. Ed.* **2013**, *24* (4), 398–416.
(31) Itaka, K.; Harada, A.; Yamasaki, Y.; Nakamura, K.; Kawaguchi, H.; Kataoka, K. In Situ Single Cell Observation by Fluorescence Resonance Energy Transfer Reveals Fast Intra-Cytoplasmic Delivery and Easy Release of Plasmid DNA Complexed With Linear Polyethylenimine. *J. Gene Med.* **2004**, *6* (2004), 76–84.
(32) Abbe, E. Beiträge Zur Theorie Des Mikroskops Und Der Mikroskopischen Wahrnehmung. *Arch. für mikroskopische Anat.* **1873**, *9*, 413–468.
(33) Huang, B.; Bates, M.; Zhuang, X. Super-Resolution Fluorescence Microscopy. *Annu. Rev.*

Biochem. **2009**, *78*, 993–1016.
(34) Godbey, W. T.; Wu, K. K.; Mikos, A. G. Tracking the Intracellular Path of Poly(Ethylenimine)/DNA Complexes for Gene Delivery. *Proc. Natl. Acad. Sci. U. S. A.* **1999**, *96*, 5177–5181.
(35) Uusitalo, J. J.; Ingólfsson, H. I.; Akhshi, P.; Tieleman, D. P.; Marrink, S. J. Martini Coarse-Grained Force Field: Extension to DNA. *J. Chem. Theory Comput.* **2015**, *11* (8), 3932–3945.
(36) Utsuno, K.; Uludağ, H. Thermodynamics of Polyethylenimine-DNA Binding and DNA Condensation. *Biophys. J.* **2010**, *99* (1), 201–207.
(37) Suh, J.; Paik, H. J.; Hwang, B. K. Ionization of Poly(Ethylenimine) and Poly(Allylamine) at Various PH′s. *Bioorg. Chem.* **1994**, *22* (3), 318–327. https://doi.org/10.1006/bioo.1994.1025.
(38) Mahajan, S.; Tang, T. Martini Coarse-Grained Model for Polyethylenimine. *J. Comput. Chem.* **2019**, *40* (3), 607–618.
(39) Mahajan, S.; Tang, T. Erratum : "Martini Coarse-Grained Model for Polyethylenimine" [J. Comput. Chem. 2019, 40, 607-618, DOI:10.1002/Jcc.25747]. *J. Comput. Chem.* **2020**, *41* (18), 1730–1734.
(40) Yesylevskyy, S. O.; Schäfer, L. V.; Sengupta, D.; Marrink, S. J. Polarizable Water Model for the Coarse-Grained MARTINI Force Field. *PLoS Comput. Biol.* **2010**, *6* (6), e1000810.
(41) Abraham, M. J.; Murtola, T.; Schulz, R.; Páll, S.; Smith, J. C.; Hess, B.; Lindah, E. GROMACS: High Performance Molecular Simulations Through Multi-Level Parallelism From Laptops to Supercomputers. *SoftwareX* **2015**, *1–2*, 19–25.
(42) De Jong, D. H.; Baoukina, S.; Ingólfsson, H. I.; Marrink, S. J. Martini Straight: Boosting Performance Using a Shorter Cutoff and GPUs. *Comput. Phys. Commun.* **2016**, *199*, 1–7. https://doi.org/10.1016/j.cpc.2015.09.014.
(43) Tironi, I. G.; Sperb, R.; Smith, P. E.; van Gunsteren, W. F. A Generalized Reaction Field Method for Molecular Dynamics Simulations. *J. Chem. Phys.* **1995**, *102* (13), 5451–5459.
(44) Verlet, L. Computer "Experiments" on Classical Fluids. I. Thermodynamical Properties of Lennard-Jones Molecules. *Phys. Rev.* **1967**, *159* (1), 98–103.
(45) Monticelli, L.; Kandasamy, S. K.; Periole, X.; Larson, R. G.; Tieleman, D. P.; Marrink, S. J. The MARTINI Coarse-Grained Force Field: Extension to Proteins. *J. Chem. Theory Comput.* **2008**, *4* (5), 819–834.
(46) Mahajan, S.; Tang, T. Meeting Experiments at the Diffraction Barrier with In Silico Fluorescence Microscopy. *ACS Photonics* **2022**. https://doi.org/10.1021/acsphotonics.1c01469.
(47) Mahajan, S. In-silico-microscopy v.1.2.2 https://github.com/subhamoymahajan/in-silico-microscopy.
(48) Gandy, R. O. Out-of-Focus Diffraction Patterns for Microscope Objectives. *Proc. Phys. Soc. B* **1954**, *67*, 825–831.
(49) Mahajan, S. NPanalysis v.1.3 https://github.com/subhamoymahajan/NPanalysis.
(50) von Smoluchowski, M. Versuch Einer Mathematischen Theorie Der Koagulationskinetik Kolloider Lösungen. *Zeitschrift f. Physik. Chemie.* **1917**, *92*, 129–168.
(51) Clamme, J. P.; Azoulay, J.; Mély, Y. Monitoring of the Formation and Dissociation of Polyethylenimine/DNA Complexes by Two Photon Fluorescence Correlation Spectroscopy. *Biophys. J.* **2003**, *84* (3), 1960–1968.
(52) Boeckle, S.; von Gersdorff, K.; van der Pipen, S.; Culmsee, C.; Wagner, E.; Ogris, M. Purification of Polyethylenimine Polyplexes Highlights the Role of Free Polycations in

Gene Transfer. *J. Gene Med.* **2004**, *6*, 1102–1111.
(53) Yue, Y.; Jin, F.; Deng, R.; Cai, J.; Dai, Z.; Lin, M. C. M.; Kung, H. F.; Mattebjerg, M. A.; Andresen, T. L.; Wu, C. Revisit Complexation Between DNA and Polyethylenimine - Effect of Length of Free Polycationic Chains on Gene Transfection. *J. Control. Release* **2011**, *152* (1), 143–151.
(54) Oishi, M.; Nagasaki, Y.; Itaka, K.; Nishiyama, N.; Kataoka, K. Lactosylated Poly(Ethylene Glycol)-SiRNA Conjugate through Acid-Labile β-Thiopropionate Linkage to Construct PH-Sensitive Polyion Complex Micelles Achieving Enhanced Gene Silencing in Hepatoma Cells. *J. Am. Chem. Soc.* **2005**, *127* (6), 1624–1625.
(55) Xiao, L.; Huang, L.; Moingeon, F.; Gauthier, M.; Yang, G. PH-Responsive Poly(Ethylene Glycol)-Block-Polylactide Micelles for Tumor-Targeted Drug Delivery. *Biomacromolecules* **2017**, *18* (9), 2711–2722.
(56) Rudolph, C.; Lausier, J.; Naundorf, S.; Müller, R. H.; Rosenecker, J. In Vivo Gene Delivery to the Lung Using Polyethylenimine and Fractured Polyamidoamine Dendrimers. *J. Gene Med.* **2000**, *2*, 269–278.
(57) Choosakoonkriang, S.; Lobo, B. A.; Koe, G. S.; Koe, J. G.; Middaugh, C. R. Biophysical Characterization of PEI/DNA Complexes. *J. Pharm. Sci.* **2003**, *92* (8), 1710–1722.
(58) Roos, A.; Boron, W. F. Intracellular PH. *Physiol. Rev.* **1981**, *61* (2), 296–434.
(59) van der Aa, M. A. E. M.; Mastrobattista, E.; Oosting, R. S.; Hennink, W. E.; Koning, G. A.; Crommelin, D. J. A. The Nuclear Pore Complex: The Gateway to Successful Nonviral Gene Delivery. *Pharm. Res.* **2006**, *23* (3), 447–459.
(60) Panté, N.; Kann, M. Nuclear Pore Complex Is Able to Transport Macromolecules with Diameters of ~39 Nm. *Mol. Biol. Cell* **2002**, *13*, 425–434.
(61) Paine, P. L.; Moore, L. C.; Horowitz, S. B. Nuclear Envelope Permeability. *Nature* **1975**, *254*, 109–114.
(62) Wang, C.; Wang, Y.; Li, Y.; Bodemann, B.; Zhao, T.; Ma, X.; Huang, G.; Hu, Z.; DeBerardinis, R. J.; White, M. A.; et al. A Nanobuffer Reporter Library for Fine-Scale Imaging and Perturbation of Endocytic Organelles. *Nat. Commun.* **2015**, *6*, 8524.
(63) Fischer, D.; Bieber, T.; Li, Y.; Elsässer, H.-P.; Kissel, T. A Novel Non-Viral Vector for DNA Delivery Based on Low Molecular Weight, Branched Polyethylenimine: Effect of Molecular Weight on Transfection Efficiency and Cytotoxicity. *Pharm. Res.* **1999**, *16* (8), 1273–1279.
(64) Godbey, W. T.; Wu, K. K.; Mikos, A. G. Size Matters : Molecular Weight Affects the Efficiency of Poly(Ethylenimine) as a Gene Delivery Vehicle. *J. Biomed. Mater. Res.* **1999**, *45* (3), 268–275.
(65) Werth, S.; Urban-Klein, B.; Dai, L.; Höbel, S.; Grzelinski, M.; Bakowsky, U.; Czubayko, F.; Aigner, A. A Low Molecular Weight Fraction of Polyethylenimine (PEI) Displays Increased Transfection Efficiency of DNA and SiRNA in Fresh or Lyophilized Complexes. *J. Control. Release* **2006**, *112* (2), 257–270.
(66) Bieber, T.; Elsässer, H. P. Preparation of a Low Molecular Weight Polyethylenimine for Efficient Cell Transfection. *Biotechniques* **2001**, *30* (1), 74–77, 80–81.
(67) Wightman, L.; Kircheis, R.; Rössler, V.; Carotta, S.; Ruzicka, R.; Kursa, M.; Wagner, E. Different Behavior of Branched and Linear Polyethylenimine for Gene Delivery In Vitro and In Vivo. *J. Gene Med.* **2001**, *3* (4), 362–372.
(68) Krämer, M.; Stumbé, J.-F.; Grimm, G.; Kaufmann, B.; Krüger, U.; Weber, M.; Haag, R. Dendritic Polyamines: Simple Access to New Materials With Defined Treelike Structures

for Application in Nonviral Gene Delivery. *ChemBioChem* **2004**, *5* (8), 1081–1087.
(69) Kondinskaia, D. A.; Kostritskii, A. Y.; Nesterenko, A. M.; Antipina, A. Y.; Gurtovenko, A. A. Atomic-Scale Molecular Dynamics Simulations of DNA-Polycation Complexes: Two Distinct Binding Patterns. *J. Phys. Chem. B* **2016**, *120* (27), 6546–6554.
(70) Maiti, P. K.; Bagchi, B. Structure and Dynamics of DNA-Dendrimer Complexation: Role of Counterions, Water, and Base Pair Sequence. *Nano Lett.* **2006**, *6* (11), 2478–2485. https://doi.org/10.1021/nl061609m.
(71) Grünewald, F.; Souza, P. C. T.; Abdizadeh, H.; Barnoud, J.; De Vries, A. H.; Marrink, S. J. Titratable Martini Model for Constant PH Simulations. *J. Chem. Phys.* **2020**, *153* (2). https://doi.org/10.1063/5.0014258.
(72) Ziebarth, J. D.; Wang, Y. Understanding the Protonation Behavior of Linear Polyethylenimine in Solutions Through Monte Carlo Simulations. *Biomacromolecules* **2010**, *11* (1), 29–38.
(73) Xu, X.; Ran, Q.; Dey, P.; Nikam, R.; Haag, R.; Ballauff, M.; Dzubiella, J. Counterion-Release Entropy Governs the Inhibition of Serum Proteins by Polyelectrolyte Drugs. *Biomacromolecules* **2018**, *19*, 409–416.
(74) Harries, D.; May, S.; Ben-Shaula, A. Counterion Release in Membrane–Biopolymer Interactions. *Soft Matter* **2013**, *9*, 9268–9284.
(75) Marrink, S. J.; de Vries, A. H.; Mark, A. E. Coarse Grained Model for Semiquantitative Lipid Simulations. *J. Phys. Chem. B* **2004**, *108* (2), 750–760.
(76) Michalowsky, J.; Zeman, J.; Holm, C.; Smiatek, J. A Polarizable MARTINI Model for Monovalent Ions in Aqueous Solution. *J. Chem. Phys.* **2018**, *149*, 163319.
(77) Mahajan, S.; Tang, T. Comment on "Martini Force Field for Protonated Polyethyleneimine." *J. Comput. Chem.* **2021**, *42* (4), 261–263. https://doi.org/10.1002/jcc.26453.
(78) Fretz, M. M.; Penning, N. A.; Al-Taei, S.; Futaki, S.; Takeuchi, T.; Nakase, I.; Storm, G.; Jones, A. T. Temperature-, Concentration- and Cholesterol-Dependent Translocation of L- and D-Octa-Arginine across the Plasma and Nuclear Membrane of CD34+ Leukaemia Cells. *Biochem. J.* **2007**, *403* (2), 335–342.
(79) Sung, L.-Y.; Chen, C.-L.; Lin, S.-Y.; Li, K.-C.; Yeh, C.-L.; Chen, G.-Y.; Lin, C.-Y.; Hu, Y.-C. Efficient Gene Delivery into Cell Lines and Stem Cells Using Baculovirus. *Nat. Protoc.* **2014**, *9* (8), 1882–1899.

For Table of Contents Use Only